Experiments and Modeling to Support Field Test Design

Fuel Cycle Research & Development

Prepared for
U.S. Department of Energy
Used Fuel Disposition Campaign
Milestone M3SF-18LA010303015

P.J. Johnson
G.A. Zyvoloski
S.M. Bourret
P.H. Stauffer

Los Alamos National Laboratory
August 31, 2018

Los Alamos National Laboratory Document
LA-UR-18-28189

FCT Quality Assurance Program Document

Appendix E
FCT Document Cover Sheet

Name/Title of Deliverable/Milestone	Experiments and Modeling to Support Field Test Design
Work Package Title and Number	**SF-18LA01030301 Salt R&D - LANL**
Work Package WBS Number	1.08.01.03.03 - Salt Disposal R&D
Responsible Work Package Manager	Philip H. Stauffer
	(Name/Signature)
Date Submitted	

Quality Rigor Level for Deliverable/Milestone	☒ QRL-3	☐ QRL-2	☐ QRL-1 ☐ Nuclear Data	☐ N/A*

This deliverable was prepared in accordance with Los Alamos National Laboratory
(Participant/National Laboratory Name)

QA program which meets the requirements of
☒ DOE Order 414.1 ☐ NQA-1-2000

This Deliverable was subjected to:

☐ Technical Review

Technical Review (TR)
Review Documentation Provided
☐ Signed TR Report or,
☐ Signed TR Concurrence Sheet or,
☒ Signature of TR Reviewer(s) below
Name and Signature of Reviewers
Hari Viswanathan

☐ Peer Review

Peer Review (PR)
Review Documentation Provided
☐ Signed PR Report or,
☐ Signed PR Concurrence Sheet or,
☐ Signature of PR Reviewer(s) below

*Note: In some cases there may be a milestone where an item is being fabricated, maintenance is being performed on a facility, or a document is being issued through a formal document control process where it specifically calls out a formal review of the document. In these cases, documentation (e.g., inspection report, maintenance request, work planning package documentation or the documented review of the issued document through the document control process) of the completion of the activity along with the Document Cover Sheet is sufficient to demonstrate achieving the milestone. QRL for such milestones may be also be marked N/A in the work package provided the work package clearly specifies the requirement to use the Document Cover Sheet and provide supporting documentation.

Table of Contents

List of Figures

List of Tables

1. Introduction

Salt repositories continue to be a primary concept for disposal of heat-generating nuclear waste (HGNW). For the past several years, efforts have focused on the in-drift disposal concept (e.g. Hansen and Leigh 2011; Stauffer et al. 2013; Jordan et al. 2015a,b,c; Bourret et al. 2016; Hansen et al. 2016; Bourret et al. 2017; Johnson et al. 2017a,b; Kuhlman et al. 2017). Ongoing research efforts aim to improve understanding of the behavior of the salt backfill surrounding HGNW sources, the responses of drift walls to heat sources, and the chemistry and chemical evolution of brine in such environments. For these purposes, a number of high-priority objectives have been identified (Stauffer et al. 2015) and are the subjects of research projects, including laboratory experiments, field-scale experiments, and numerical simulations (e.g. Jordan et al. 2015a,b,c; Bourret et al. 2016; Rutqvist et al. 2016; Bourret et al. 2017; Johnson et al. 2017a,b; Kuhlman et al. 2017; Rutqvist et al. 2017). Verification and validation of numerical models remain an essential component of this research.

Work conducted by LANL for Salt R&D during the 2018 fiscal year includes a series of preliminary borehole experiments (Johnson et al. 2017b), numerical modeling for generic repository science with potential international applicability, and fundamental code development. The first two of these focus areas are the subject of separate milestones (M3SF-18LA010303014 and M4SF-18LA010303041). The remaining FY18 Salt R&D work performed by LANL is summarized in this report and focuses primarily on development, implementation, and testing of code for the porous flow simulator FEHM (Zyvoloski et al. 2012, https://fehm.lanl.gov).

Following Johnson et al. (2017a), model development efforts focused on the implementation and testing of a function for capillary pressure with variable porosity (CPVN;

Figure 1-1). A manuscript of this work is, at the time of this writing, under review for publication in Transport in Porous Media and is reproduced in Appendix C of this milestone. That function took a final form of:

$$P_c = P_{cmaxi}\left(\frac{1-n}{1-n_i}\right), \qquad S_l \le S_{ri}\frac{1-n}{1-n_i}$$

$$P_c = P_{cmax}\frac{S_{lmax}-S_l}{S_{lmax}-S_{ri}\frac{1-n}{1-n_i}}, \qquad S_{ri}\frac{1-n}{1-n_i} < S_l < S_{lmax} \qquad \text{Eq. 1}$$

$$P_c = 0.0, \qquad S_l \ge S_{lmax}$$

Where P_c is capillary pressure (MPa), P_{cmax} is the maximum capillary pressure at low saturation, S_r is the residual saturation, S_{lmax} is the maximum saturation above which capillary pressure is zero, n is porosity, S_l is the current liquid saturation, and the subscript *i* denotes the initial user-specified value which is then recalculated during the model run. By varying the residual saturation and modifying the capillary retention curve, model behaviors can be avoided that do not make physical sense, such as the partial saturation of open air nodes.

An additional function based on Leverett (1941) has recently been implemented (see Appendices A and B). This milestone is, therefore, composed of descriptions and testing of the Leverett function as well as other minor code amendments and tests.Appendix C describes development of the CPVN capillary function, as submitted for publication..

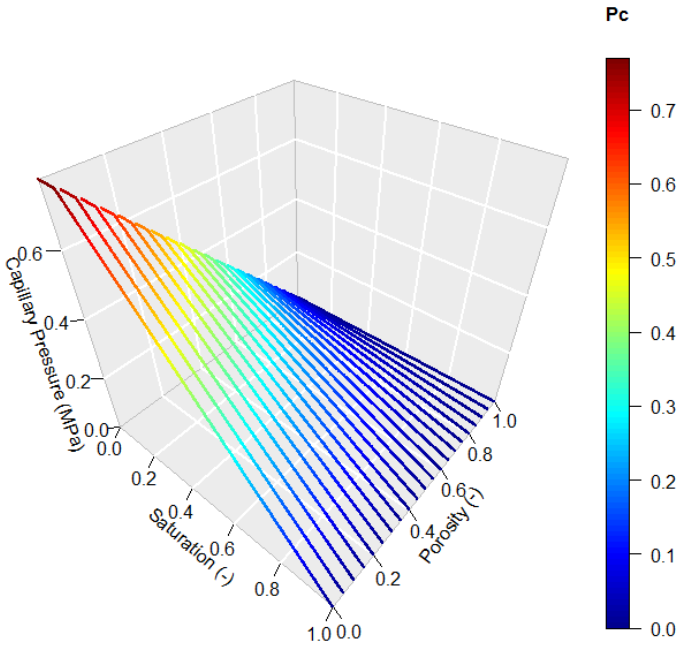

Figure 1-1: 3-D plot of CPVN function, with capillary pressure (vertical access) as a function of porosity and saturation.

2. FEHM Updates

2.1 Code modifications

The primary FEHM code developments were applied to the cappr.f function to add the CPVN and Leverett capillary functions. A few minor changes were applied to other subroutines, in order to handle new model inputs. Usage of the Leverett function is presented in Appendix A, and code changes within cappr.f can be found in Appendix B.

Table 2-1: FEHM subroutines to which salt-relevant code modifications have been applied.

Subroutine	Description of change
allocmem.f	Allocated arrays needed for Leverett permeability tracking
cappr.f	Added Leverett function and minor fixes to CPVN function (see Appendix B)
comdi.f	Added common variables for Leverett function
rlperm.f	Added flag, definitions, and reads for Leverett function
saltctr.f	Added permeability tracking for Leverett function
vcon.f	Adjusted thermal conductivity function to decrease with porosity above 0.4

3. Implementation and Testing of Leverett Retention Function

3.1 Background

The successful implementation of the CPVN function (Johnson et al. 2017a; see Appendix C) demonstrates the necessity of properly accounting for changing porosity in the multiphase salt systems. Another CPVN function, without the ability to modify residual saturation as a function of porosity, can be found in Leverett (1941) and its implementation within TOUGH-FLAC,

$$P_{cmax} = P_{cmaxi} \frac{\sqrt{k/n}}{\sqrt{k_i/n_i}} \quad \text{Eq. 2}$$

where Pcmax is the maximum capillary pressure, *k* is permeability (m^2), and *n* is porosity. The subscript *i* indicates the initial value for the medium, with porosity and permeability updating during the course of the simulation. The Leverett function therefore relates porosity, permeability, and capillary pressure in similar rocks within a reservoir, assuming comparable pore shapes. Based on this function, the ratio $\sqrt{k/n}$, is interpreted to relate to the mean pore radius in a bundled capillary tube model, where *k* is the permeability of the porous medium and *n* is porosity (Rutqvist et al. 2002). In the context of salt, it is unclear whether the assumption of consistent pore structure applies across the full range of potential porosity values, a drawback of both the Leverett function and the linear CPVN function. In the interest of comparing the capillary models, the Leverett function has been implemented in FEHM and modified to account for changing residual saturation, which has not been taken into account in the generic Leverett function or within TOUGH-FLAC.

3.2 Residual saturation

A potential problem with applying the Leverett capillary function to salt models is that it retains a capillary pressure at high porosity. As noted in Johnson et al. (2017a), allowing for

non-zero capillary pressures in model domains with increasing porosity can cause the model to behave in unrealistic ways, including the retention of water in void spaces due to capillary action despite the absence of a porous medium. One aspect of this problem is in the residual saturation (S_r) value, which is not incorporated in the general Leverett function but is a term within the general capillary retention function described in Rutqvist et al. (2002). For example, if S_r is fixed at 0.1 for a model run with initially low porosity, S_r will still be 0.1 even if porosity increases to 0.9999. Consequently, the model will predict the maximum capillary pressure at any location with a saturation at or below 0.1; even a node at n = 0.9999 will tend to maintain saturation near the residual value of 0.1. Consequently, volumetric water content ($\theta = nS$) will be very high due to capillary effects, even though there is no porous medium available on which capillary effects to act. Conversely, as porosity decreases to near zero, the wetting phase should tend to be strongly retained. Part of this behavior is incorporated in the strong increase in the Leverett function capillary pressure at low porosity, but the residual saturation value should also increase (Buckles, 1965; Holmes et al. 2009).

In light of the aforementioned issues, we have elected to include an option for changing residual saturation in the implemented Leverett function in FEHM. If the user chooses to use a constant value, then the fixed user-entered S_r value is maintained throughout the simulation. Otherwise, a linear function is applied following Johnson et al. (2017a), with decreasing S_r as porosity increases and increasing S_r as porosity decreases. This allows for a reduction in saturation values at very high porosity relative to the unmodified Leverett function while also increasing saturation in remaining tight pores as porosity decreases. The linear extrapolation for very low porosity prevents model convergence issues that could be present if nonlinear approaches are applied.

3.3 Verification of the new CPVN functioin

3.3.1 8 Node Problem

Following Johnson et al. (2017a), an 8-node FEHM simulation problem was constructed to test how variable temperatures allow for small changes in porosity and permeability of the medium. Properties appropriate for crushed granular salt are applied with the Leverett function parameters (see Appendix A) as shown in Table 3-1 and the salt macro is active to generate changing porosity values. No external sources or sinks of water or gas are applied. Residual saturation was allowed to vary as a function of porosity. For this test run, an additional file was output containing the model permeability, porosity, maximum capillary pressure, and calculated capillary pressure at each iteration. This file is not normally output in FEHM but allows investigation of internal calculations in the software.

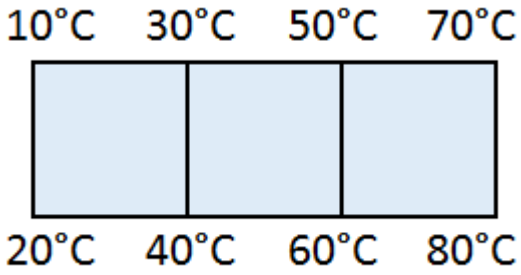

Figure 3-1: Model domain for 8-node problem.

Table 3-1: Starting parameters for test of Leverett function.

Parameter	Value
Initial porosity (-)	0.35
Initial permeability (m^2)	10^{-12}
Initial maximum capillary pressure (MPa)	0.05
Residual saturation (-)	0.1

Figure 3.2 shows results for analytical and numerical simulations. The calculated Leverett function (Figure 3.2-A) is analytically derived based on Eqn. 2 and follows porosity.

Note that permeability calculations are produced within the salt macro, independently of the capillary function. Figure 3.2-B shows the calculation of porosity-variable residual saturation (S_r) when the option is applied. An initial value of 0.1 was used in this simulation. Porosity variations are minor, so little change occurs in the calculated S_r value, but the expected analytical value based on internal FEHM variables and the calculated value match precisely. Likewise, the calculated Leverett maximum capillary pressure (P_{cmax}) and final saturation-fit capillary pressure (P_c) both match their expected analytical values. Based on these close fits, the Leverett function has been correctly implemented in the code and is reproducing the correct values based on variables passed to the cappr.f subroutine from elsewhere in FEHM.

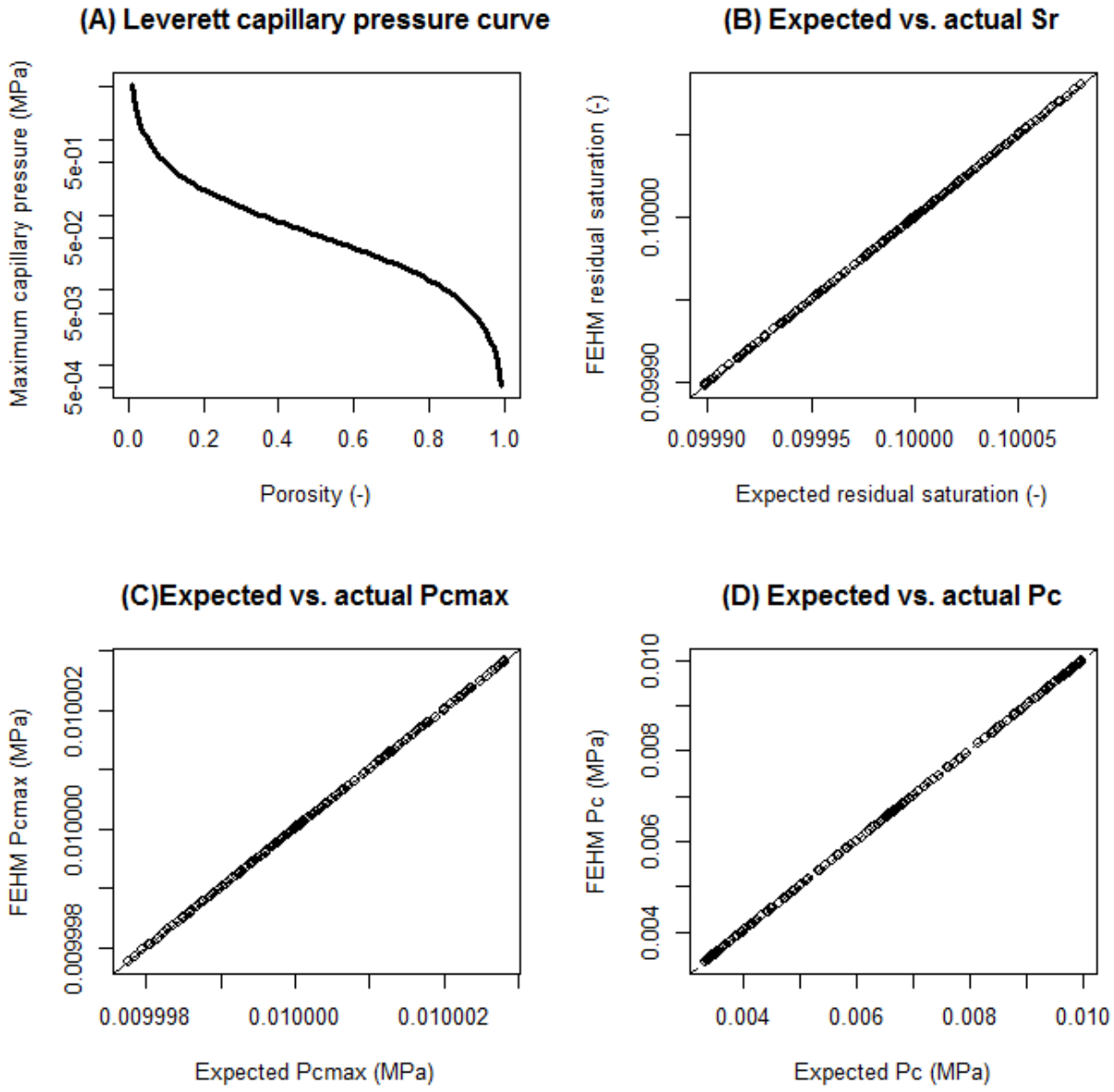

Figure 3-2: (A) Calculated maximum capillary pressure based on Leverett function. (B) Residual saturation as calculated in FEHM on 8-node problem compared to expected value with same inputs. (C) Maximum capillary pressure as calculated in FEHM on 8-node problem compared to expected value with same inputs. (D) Calculated capillary pressure with saturation fit as calculated in FEHM on 8-node problem compared to expected value with same inputs. For (B), (C), and (D), a 45° line is included and points match to within the limits of the data storage type.

4. Comparison of Leverett and CPVN functions

With the successful implementation of the Leverett function and the prior work described in Johnson et al. (2017a), the following subsections present tests to evaluate the effect and performance of the Leverett functions compared to the new CPVN porosity-dependent retention

function. In light of the relative lack of experiments with changing-porosity salt domains, some of this work must be conceptual. We therefore consider first the differences between the two functions, then simulate the previously-examined (Bourret et al. 2016; Johnson et al. 2017a; Blanco-Martin et al. 2018) experiments of Olivella et al. (2011), and finally examine a larger-scale model domain. Two general questions are considered:

(1) How different are the simulation results at different scales?

(2) How does the efficiency of the two approaches compare at different scales?

We further note that the larger-scale test problems do not have identified correct answers, complicating identification of a "better" function. In both cases we also aim to identify whether clearly unrealistic model behaviors are occurring.

4.1 Example calculations

Inputting a sample set of numbers for the Leverett and CPVN functions allows comparison of the relative strength of the calculated maximum capillary pressure produced by each function from the same starting conditions. Figure 4-1 shows the range of porosity from 0.1 to 1.0 compared to the maximum capillary pressure for each function. The Leverett function tends to be relatively weak compared to the linear CPVN formulation as porosity increases. Conversely, as porosity decreases, the Leverett function produces far stronger capillary pressure, and an exponential increase in capillary pressure as porosity draws closer to zero. Although theory suggests that such a strong increase is feasible based on conceptual models such as bundled capillary tubes (e.g. Masoodi and Pillai 2012), some uncertainty remains as to the applicability, relevance, and physical correctness of such a function to a changing-porosity medium. Furthermore, as described in subsequent sections, the exponential increase in capillary

pressure as porosity approaches zero causes numerical difficulties that complicate application of the model to large domains.

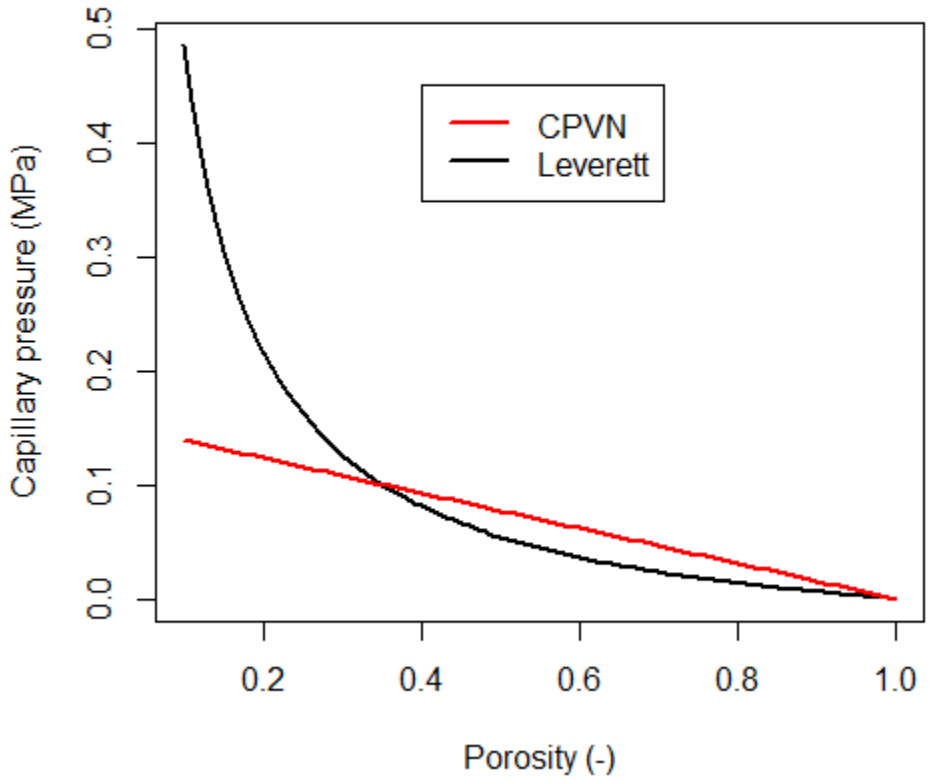

Figure 4-1: Maximum capillary pressure as function of porosity in CPVN (red line) and Leverett functions. Leverett maximum capillary pressure diverges as porosity approaches 0.

4.2 Test problem 1: Olivella experiment simulations

The experiments by Olivella et al. (2011) consisted of a 10 cm long tube filled with fine granular salt. One end of the tube was heated to 85°C and the other cooled to 5°C. Previous discussions of the experiment have been presented in several milestones (Bourret et al. 2016; Johnson et al. 2017a) and elsewhere (e.g. Blanco-Martin et al. 2018). The present work does not aim to add to the discussion of physical processes as learned from this experiment. Instead, the previous modeling work presents a readily available test case for the new Leverett function,

results from which can be compared to a simple, non-porosity-dependent retention function and the CPVN function.

Based on the experiment, a simple model domain is constructed with a 10 cm long, 3 cm tall mesh of uniform 1 cm spacing. A uniform starting porosity of 0.3 and saturation of 0.3 is applied, along with thermal boundaries of 85°C and 5°C. 65 days of time are simulated with the salt macro active. Porosity results after 65 days are shown in Figure 4-2. Results using the Leverett function are in close agreement with the other models, indicating that the new function is working properly and does not strongly change the simulation results at this small scale.

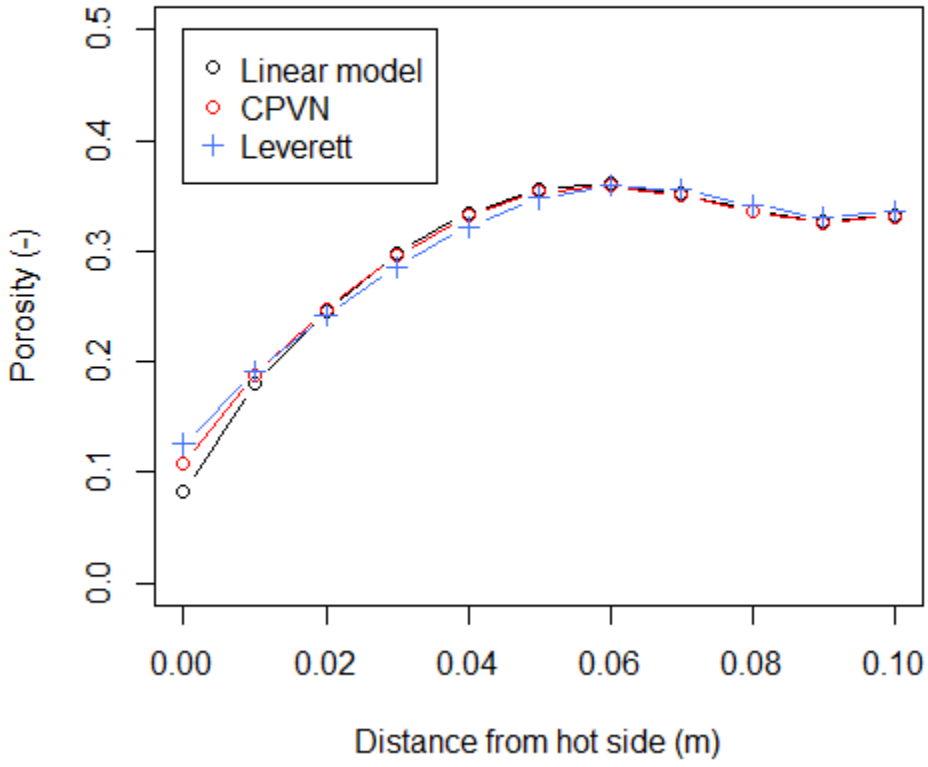

Figure 4-2: Simulated porosity after 65 days in domain based on Olivella et al. (2011). Results with Leverett function (blue crosses) are similar to those of linear and CPVN functions as noted in Johnson et al. (2017a).

4.3 Test problem 2: Square box

The second test problem applies the Leverett function to a thought experiment (described in more detail in Appendix C) with a 10x10 m square box (Figure 4-3). Material in the box is simulated as crushed salt, with an initial porosity of 0.3. A fixed temperature of 25°C is applied to the top and right-hand (x = 10 m) edges of the box, while the bottom and left-hand (x = 0) boundaries are considered no-flow (Neumann) boundaries with respect to heat and mass. Pressure is fixed at atmospheric (0.1 MPa) along the top boundary. A 120 °C fixed temperature is applied to a node 3 m above the lower left corner. Initial temperature within the box is set to 25 °C, with heat flow away from the 120 °C node gradually heating the box interior. Gas and brine flow allows the porosity and permeability of different areas of the box to increase or decrease as brine evaporates or vapor condenses. The box is initially saturated in the bottom 8 meters. Gravity is enabled for these simulations. Each simulation is run for 125 days, the duration attained by the Leverett function simulations within 24 hours of run time (see Section 3.4 for a discussion of function efficiency).

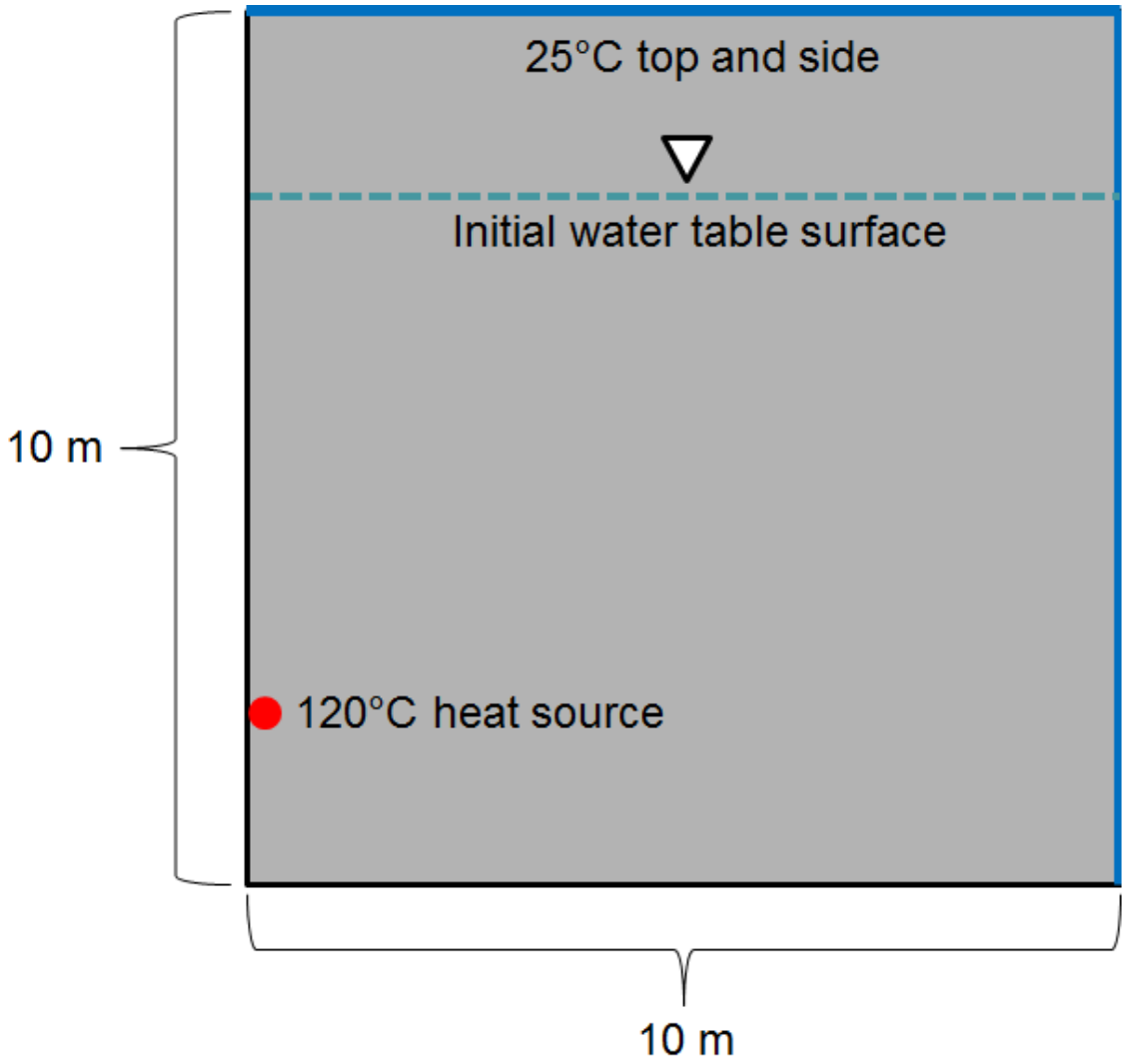

Figure 4-3: Model domain for 10 m x 10 m square box at initial conditions. Top and right boundaries are held constant at 25°C.

Three simulations were conducted with different capillary retention functions: (1) a fixed, saturation-only function; (2) the CPVN; and (3) the newly implemented Leverett function. A discussion of the relative effects of the saturation-only and CPVN functions may be found in Appendix C. For the present discussion, we focus on the comparison of simulated porosity changes using the Leverett and CPVN function (Figure 4-4).

Porosity changes from the two functions are broadly comparable, in that a region of low porosity forms near the heat source and a region of increased porosity forms at some distance

away from the heat source where condensation occurs. An additional area of decreased porosity develops beyond the dissolution zone where brine drawn from the condensation region by capillary action cools and the solubility of salt decreases, causing precipitation. However, clear differences in model behavior may be observed when the Leverett function is applied. A much broader area is subjected to dissolution and porosity increases. Rather than a general band, small clusters of a few nodes develop high porosities while adjacent clusters of nodes are relatively unaffected. Near the bottom of the box, the dissolution region extends farther from the heat source and covers a wider area. Precipitation at the heat source is much more localized, with only a few nodes decreasing in porosity. At this larger scale, the Leverett and CPVN functions show considerable differences in output, suggesting that a detailed assessment of the large-scale capillary behavior of run-of-mine salt would be useful for the future.

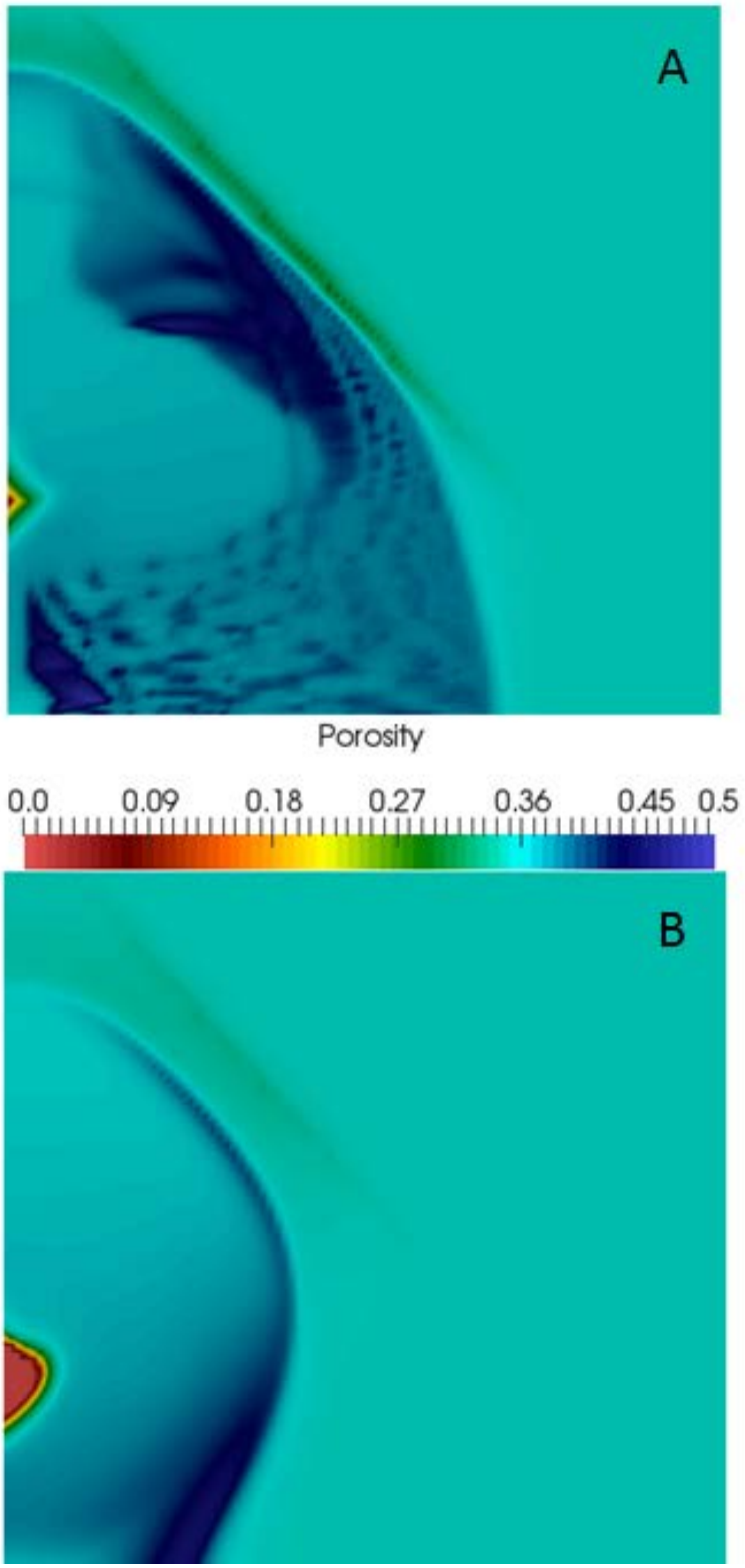

Figure 4-4: Porosity after 125 days using Leverett functions (A, top) and CPVN function (B, bottom).

4.4 Comparison of function efficiency

In addition to the simulation results, we also evaluate the model performance in terms of the efficiency and time required to apply each function. This evaluation is conducted based on the amount of iterations, timesteps, and restarted timesteps in each simulation. Results for the test problems are shown in Tables 4-1 and 4-2. In each test problem, the Leverett function is compared to the CPVN function and a simple linear, saturation-only retention function.

Timesteps are the number of separate periods of simulation time needed to complete the specified total run time in a transient model. Thus, each timestep represents a certain period of simulated time. An increase in the number of timesteps when different functions are applied, given the same timestep control inputs, indicates that convergence is more difficult and shorter timesteps must be run to achieve a solution. If the model is unable to converge to the given tolerance, the timestep restarts with a smaller increment. Numerous restarts indicate that the code is unable to apply a large timestep and is having difficulties converging. In salt models, timestep restarts often occur if the step size increases such that large porosity changes may be occurring within nodes during the step.

Two types of iterations are used in FEHM, namely outer Newton-Raphson (N-R) iterations and an inner solver iterations. At the beginning of each timestep, the code makes an initial guess at what the answer will be. This guess is based on the derivative of the change of a given term with respect to another variable, times the change in that variable. Therefore, each timestep will contain at least one N-R iteration; if a timestep is restarted, an additional N-R iteration will occur. In addition, if timestep convergence is not achieved within a user-specified number of solver iterations, the model will again take the derivatives of all functions, make a

new guess at the condition, and the process repeats. Thus, an increase in the number of N-R iterations indicates that the initial solution guess is far from the final solution.

Once the initial guess has been made in the N-R iteration, the model then uses a solver algorithm through a series of iterations to determine its final answer for the timestep, with the final answer achieved when the residuals of the conservation equations are within user-specified tolerances. The number of solver iterations required will therefore depend on the convergence criteria specified by the user, the nearness of the initial guess, and the variability found within the model. Given equal convergence criteria, greater numbers of solver iterations indicate greater difficulty in achieving a solution.

Table 4-1: Olivella experiment results

Capillary model	Linear	CPVN	Leverett
Timesteps	95	95	97
N-R iterations	114	275	258
Solver iterations	2,663	3,508	7,278
# Restarted timesteps	0	0	0

Table 4-2: Square box results

Capillary model	Linear	CPVN	Leverett
Timesteps	3,983	2,702	11,028
N-R iterations	15,737	14,429	42,082
Solver iterations	146,881	606,283	1,649,997
# Restarted timesteps	421	299	1244

From the results listed in Tables 4-1 and 4-2, it is clear that the currently implemented form of the Leverett capillary function is highly inefficient compared to both the fixed saturation-only function and the CPVN function, although both porosity-dependent functions have greater difficulty converging than the saturation-only function. A challenge faced by both porosity-dependent functions is that the initial solution guess from the N-R iterations is made

without *a priori* knowledge of what the porosity solution will be as passed from the tracer and reaction sub-routines of FEHM. Thus, the initial guess is typically far enough from the final solution in active (changing-porosity) nodes to require many additional solver iterations before convergence is achieved. The fixed, saturation-only function does not encounter these difficulties to the same extent because the same linear fit of saturation is always applied. Consequently, the same derivative function is always applicable. In the porosity-dependent functions, the derivative used in the initial guess for the next timestep is based on the linear fit of the previous timestep, but as porosity changes the actual interpolated line also changes, resulting in a guess that is far from the final solution.

The Leverett function is likely much less efficient than the CPVN function because of the exponential increase in capillary pressure at low porosity. Significant increases in maximum capillary pressure at low porosity results in a very steep pressure-saturation gradient. Small changes in the saturation value from the solver algorithm result in very large pressure differences in a low-porosity node, which must then be balanced against adjacent nodes. Consequently, many more solver iterations are required to narrow down a solution to the convergence criteria. Furthermore, a value passed from an iteration might then cause an adjacent node to attain a value that is out of bounds of the model (e.g. a negative temperature or saturation), causing a restart of the timestep. An improved derivative formulation within the Leverett function is necessary before this function can be successfully implemented in large-scale problems, because the current inefficiency would cause large-scale models to be prohibitively time consuming and expensive in computing power.

4.5 Summary

At the time of this milestone, the retention function based on Leverett (1941) and its numeric implementation Rutqvist et al. (2002) have been implemented in FEHM. Small-scale test problems indicate the function is correctly calculating capillary pressure and produces comparable results to previous simulations of the Olivella et al. (2011) experiments. However, in large computational domains where porosity approaches zero, the function produces strongly different results from the previous models, leaving unresolved whether the function represents an improvement in numeric technique. In addition, the implemented Leverett function is highly inefficient and time consuming. Further refinement of the derivative function is necessary before large-scale application of this function can be applied. Until this is solved, the CPVN function or a similar, simple porosity-dependent retention function is available for changing-porosity salt problems.

5. Check of Thermal Conductivity Function

5.1 Background

Thermal conductivity in salt changes as a function of both temperature (Munson et al. 1990) and porosity (Gable et al. 2009). Numerical simulators account for this variability by assigning a scaled polynomial function. Porosity effects typically follow Gable et al. (2009) based on experimental results presented in (Bechthold et al. 2004), with a fourth order polynomial,

$$\kappa_{T-ASSE}(n) = -270n^4 + 370n^3 - 136n^2 + 1.5n + 5 \qquad \text{Eq. 3}$$

Where κ is thermal conductivity (W/mK) based on data from the Asse Salt Mine in Germany and n is porosity. As defined, the function is a best-fit curve based on experimental data, but does not necessarily reflect a broader physical meaning in terms of utilizing a fourth-order

polynomial. A plot of this equation (Figure 5-1) shows clearly unphysical behaviors above a porosity of about 0.4; thermal conductivity should not increase with increasing porosity from between porosities of about 0.4 and 0.6. Even more problematic, this polynomial calculates negative thermal conductivity which is a physical impossibility. The function behaves in this manner because the data used in the polynomial fit were only for porosities ranging from 0.1 to 0.4 (Gable et al. 2009).

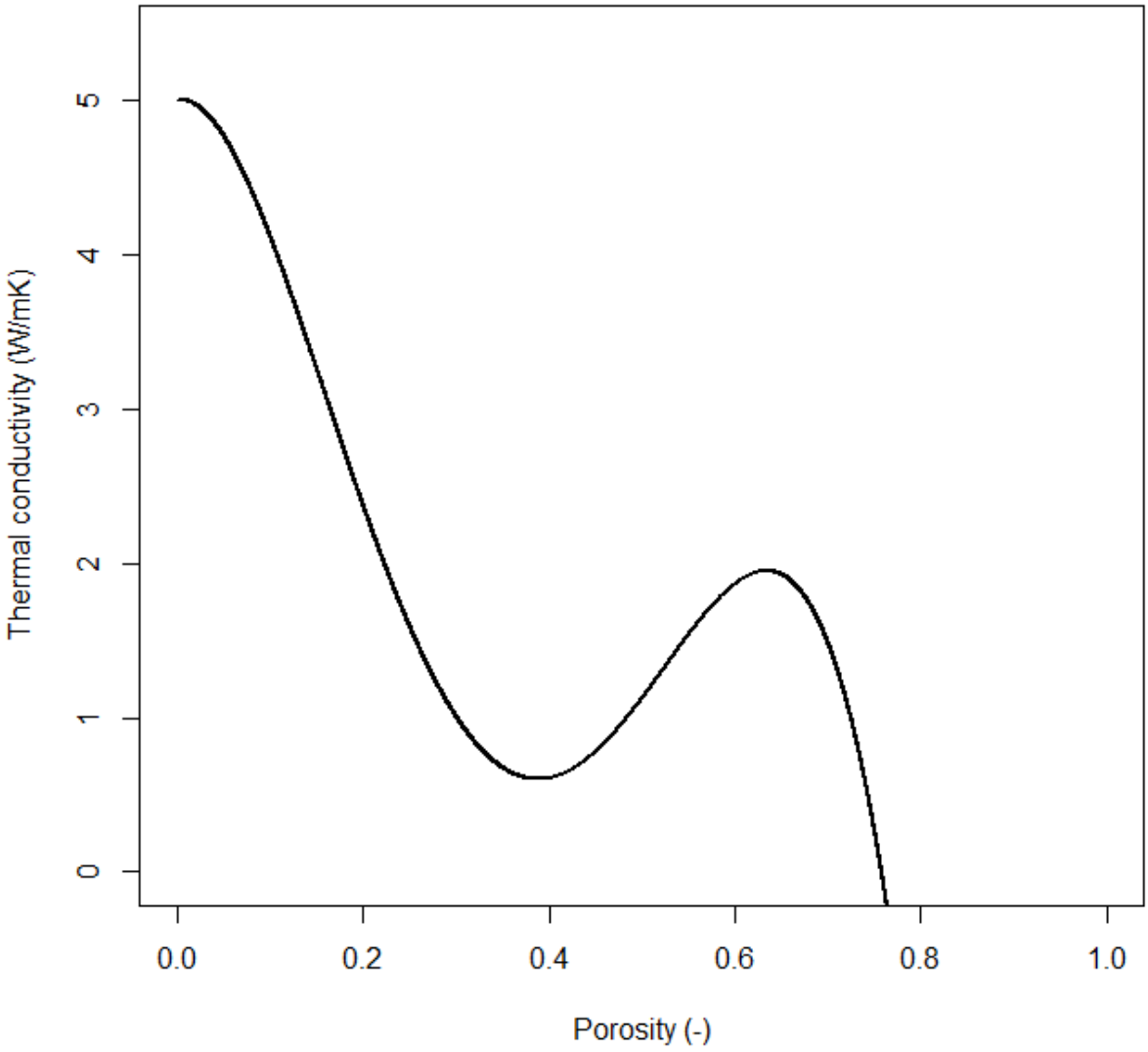

Figure 5-1: Thermal conductivity as function of porosity based on Gable et al. (2009), with no correction made for unphysical model behaviors at high porosity.

Both TOUGH-FLAC and prior implementations of FEHM applied a truncation to the thermal conductivity-porosity function above $n = 0.4$ by simply holding the thermal conductivity constant at the value of the local minimum around $n = 0.4$. Although this fix is clearly an improvement over the polynomial function, it still yields a thermal conductivity value that over-predicts thermal conductivities at high porosity. This effect can be seen most clearly at

porosities near 1, where the applied truncation yields at thermal conductivity of about 0.6 W/mK instead of the thermal conductivity of air, roughly 0.03 W/mK. As such, conductive heat transfer may be overestimated by up to an order of magnitude in increasing-porosity salt domains.

Unfortunately, experimental data are sparse concerning the proper thermal conductivity function to apply to increasing-porosity domains. Early experiments (e.g. Bechthold et al. 2004) did not measure heat transfer for any high-porosity salt media. Although Olivella et al. (2011) reported porosity values well above 0.4 in their experiment, temperature and heat transfer data were not recorded. Consequently, the exact extrapolation of the conductivity function with respect to porosity above 0.4 is unknown.

5.2 Modified Thermal Conductivity Function Description

We have implemented a simple linear extrapolation of the thermal conductivity function into a test code of FEHM. For porosity values less than about 0.39, the fourth-order polynomial function of Gable et al. (2009) is applied. Starting at the local minimum ($\kappa \approx 0.6$ W/mK at $n = 0.39$), conductivity decreases linearly until porosity increases to 1.0, at which point the final thermal conductivity value of air is applied. This yields a thermal conductivity curve that is steepest at very low porosity and slowly decreases at high porosity (Figure 5-2). The present work does not aim to present a final thermal conductivity function, rather the following test problem is designed to identify whether simulated temperature differences with the decreasing thermal conductivity function are great enough to merit further investigation of this topic.

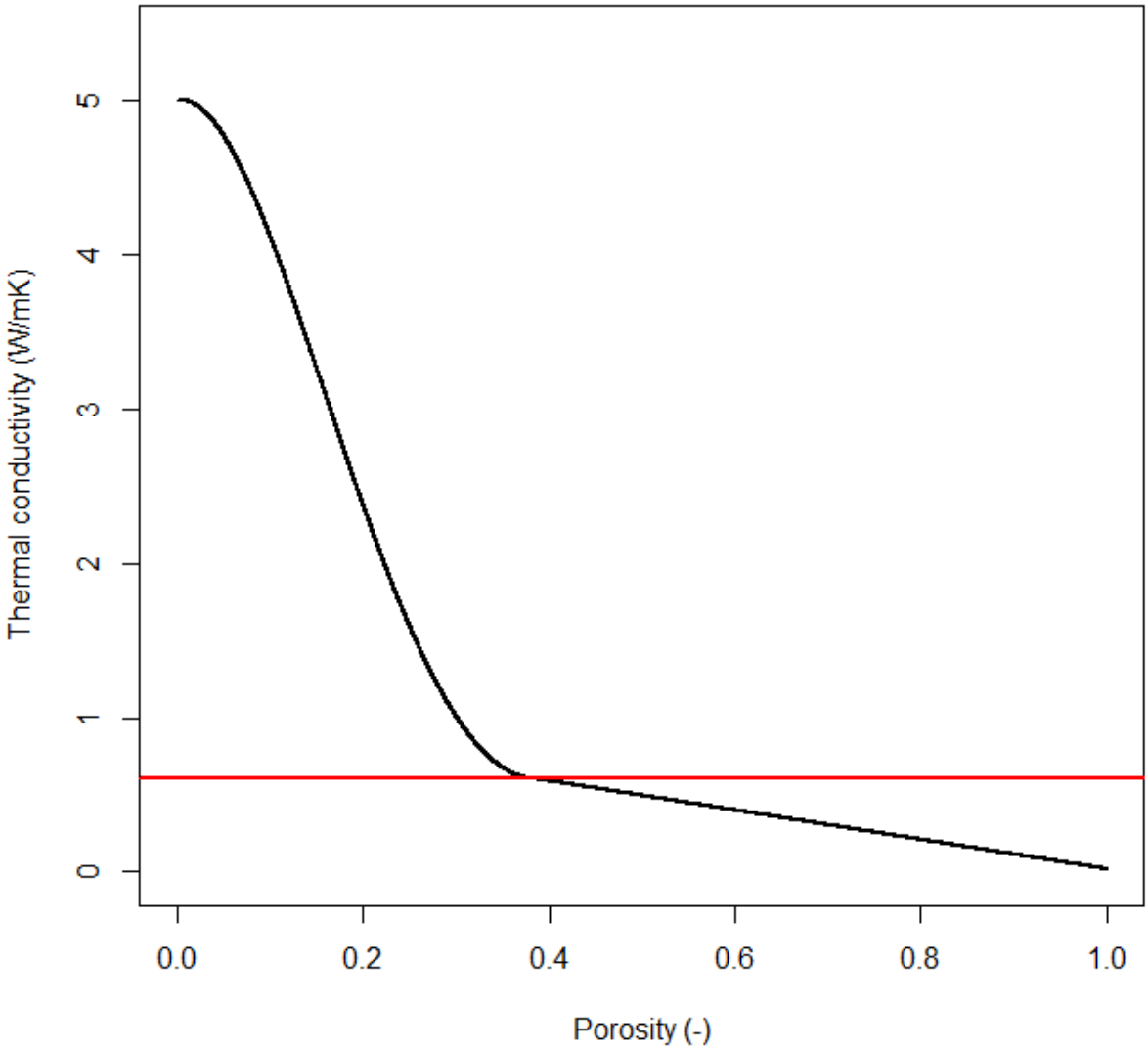

Figure 5-2: Corrected thermal conductivity relationship to porosity. Previous versions and Blanco-Martin et al. (2018) use a constant function above porosity of about 0.395

5.2.1 Test Problem

An up-scaled domain, based on the simulations of the Olivella experiment described in Section 4.2, with the salt cylinder expanded to 1 m in length and a temperature of 110 °C applied at the hot end was simulated to test the thermal conductivity function. Simulations are run for

1000 days, allowing enough time for porosity changes above the n = 0.4 threshold for the new function, so that the effects of the conductivity functions can be examined.

We compare porosity and temperature results from the old, constant conductivity function and the new, function that decreases thermal conductivity as porosity increases above 0.4. Results are comparable between the two runs, with a slight increase in the width of the dissolution band at roughly the midpoint (0.5 m) of the cylinder when the new function is applied. A slightly higher temperature occurs in the new model through the high-porosity zone. All temperatures in the simulation are within 2 °C of each other, indicating that this is a minor effect in this test problem. Given the high variability of materials in salt repository systems, the magnitude of uncertainty induced by the thermal conductivity function may be small compared to other sources of error and uncertainty. Nevertheless, a future study of the porosity and thermal conductivity relationship across the entire porosity range will be beneficial to improve confidence in the model function.

6. References

Bechtold, W., Smallos, E., Heusermann, S., Bollingerfehr, W., Bazargan-Sabet, B., Rothfuchs, T., Kamlot, P., Gnupa, J., Olivella, S., Hansen, F.D. Backfilling and sealing of underground repositories for radioactive waste in salt (BAMBUS II Project). EUR 20621 EN, European Commission (2004).

Bourret, S.M., Johnson, P.J., Zyvoloski, G.A., Chu, S.P., Weaver, D.J., Otto, S., Boukhalfa, H., Caporuscio, F.A., Jordan, A.B., Stauffer, P.H. Experiments and modeling in support of generic salt repository science. Los Alamos National Laboratory, USDOE Used Fuel Disposition Campaign Final Report (2016), LA-UR-16-27329.

Bourret, S.M., Otto, S., Johnson, P.J., Weaver, D.J., Boukhalfa, H., Stauffer, P.H. High level waste in salt repositories: Experiments and simulations of evaporation in the underground. Waste Management 2017 Proceedings (2017).

Buckles, R.S. Correlating and averaging connate water saturation data. Journal of Canadian Petroleum Technology 9(1), 42-52 (1965).

Cinar, Y., Pusch, G., Reitenbach, V. Petrophysical and capillary properties of compacted salt.

Transport in Porous Media 65(2), 199-228 (2006).

FEHM (2017), FEHM Website, https://fehm.lanl.gov/ accessed Jan 11, 2017.

Gable, C.W., Clayton, D.J., Lu, Z. Inverse modeling to determine thermal properties of salt due to heating from high level waste emplaced in a generic salt repository. US DOE Office of Nuclear Fuel Recycling Report AFCI-WAST-PMO-DV-2009-000001 (2009).

Hansen, F.D., Sobolik, S. and P.H. Stauffer, (2016). *Intermediate Scale Testing Recommendation Report*, SAND2016-9041R, FCRD-UFD-2016-000030, Albuquerque, NM: Sandia National Laboratories.

Harp, D.R., Stauffer, P.H., Mishra, P.K., Levitt, D.G., Robinson, B.A. Modeling of high-level nuclear waste disposal in a salt repository. Nuclear Technology 187:294-307 (2014). Doi:10.13182/NT13-110

Holmes, M., Holmes, A., Holmes, D. Relationship between porosity and water saturation: methodology to distinguish mobile from capillary bound water. AAPG Annual Convention and Exhibition, Denver, CO (2009).

Johnson, P.J., Bourret, S.M., Boukhalfa, H., Caporuscio, F.A., Zyvoloski, G.A., Weaver, D.J., Otto, S., Stauffer, P.H. Experiments and modeling to support field test design. Los Alamos National Laboratory, USDOE Fuel Cycle Research & Development Final Report (2017), LA-UR-17-27759.

Jordan, A.B., Boukhalfa, H., Caporuscio, F.A., Stauffer, P.H. Brine Transport Experiments in Run-of-Mine Salt. Los Alamos National Laboratory Report (2015a), LA-UR-15-26804.

Jordan, A.B., Zyvoloski, G.A., Weaver, D.J., Otto, S., Stauffer, P.H. Coupled Thermal-Hydrologic-Chemical Model for In-Drift Disposal Test. Los Alamos National Laboratory Report (2015b), LA-UR-15-27442.

Jordan, A.B., Boukhalfa, H., Caporuscio, F.A., Robinson, B.A., Stauffer, P.H. Hydrous Mineral Dehydration around Heat-Generating Nuclear Waste in Bedded Salt Formations. Environmental Science & Technology, 5:1-13 (2015c). DOI: 10.1021/acs.est.5b01002.

Kuhlman, K.L., Malama, B. Brine Flow in Heated Geologic Salt. Sandia National Laboratories Report SAND2013-1944 (2013).

Leverett, M.C. Capillary Behavior in Porous Solids. Society of Petroleum Engineers 142(1) (1941). Doi:10.2118/941152-G

Masoodi, R., Pillai, K.M. A general formula for capillary suction-pressure in porous media. Journal of Porous Media 15(8), 775-783 (2012), DOI: 10.1615/JPorMedia.v15.i8.60.

Olivella, S., Castagna, S., Alonso, E.E., Lloret, A. Porosity variations in saline media induced by temperature gradients: experimental evidences and modeling. Transport in porous media, 90(3): 763-777 (2011).

Rutqvist, J.L., Martin, B., Molins, S., Trebotich, D., Birkholzer, J. Modeling coupled THM processes and brine migration in salt at high temperatures. UFD Document FCRD-UFD-2015-000366, LBNL-191216 (2016).

Rutqvist, J., Hu, M., Blanco-Martín, L., and Birkholzer, J., 2017. *Coupled THM Modeling in Support of a Phased Salt Field Test Plan*. Lawrence Berkeley National Laboratory, SFWD-SFWST-2017-000103, LBNL-2001023, Berkeley, CA.

Stauffer, P.H., Harp, D.R., Jordan, A.B., Lu, Z., Kelkar, S., Kang, Q., Ten Cate, J., Boukhalfa, H., Labyed, Y., Reimus, P.W., Caporuscio, F.A., Miller, T.A., Robinson, B.A. Coupled model for heat and water transport in a high level waste repository in salt. Los Alamos National Laboratory, DOE Level 2 Milestone FCRD-UFD-2013-000206 (2013), LA-UR-13-27584.

Stauffer, P.H., Jordan, A.B., Weaver, D.J., Caporuscio, F.A., Ten Cate, J.A., Boukhalfa, H., Robinson, B.A., Sassani, D.C., Kuhlman, K.L., Hardin, E.L., Sevougian, S.D., MacKinnon, R.J., Wu, Y., Daley, T.A., Freifeld, B.M., Cook, P.J., Rutqvist, J., and Birkholzer, J.T., 2015. *Test proposal document for phased field thermal testing in salt*. Los Alamos National Laboratory, FCRD-UFD-2015-000077, Los Alamos, NM.

Zyvoloski, G.A., Robinson, B.A., Dash, Z.V., Kelkar, S., Viswanathan, H.S., Pawar, R.J., Stauffer, P.H., Miller, T.A., Chu, S.P. Software users manual (UM) for the FEHM Application Version 3.1-3.X, LANL Report (2012), LA-UR-12-24493

7. Appendix A: Usage and description of Leverett Function and updated CPVN function

Usage and sample model inputs for the new capillary retention functions are collated here. All specifications go under control statement *rlp*. The user inputs the model number as either -666 or -333, depending which model is desired.

For the -666 CPVN model, several additional integers are built into the input reading that are for model functions that are not yet implemented. These include a potential modification of the maximum saturation above which capillary pressure goes to zero, where the user in a future implementation could allow a changing maximum saturation with a minimum possible value. In addition, as discussed in Johnson et al. (2017a), a potential amendment to the residual saturation function based on the formulation of Buckles (1965) and subsequent revision by Holmes et al. (2009) may be applied in the future, based on

$$\alpha = S_r^q n$$

where α is constant and q is an experimentally-determined or estimated parameter.

The input parameters differ between the two models so for clarify two separate variable lists follow, first for the CPVN function and then the Leverett function.

Control statement rlp (optional)

Group 1 – IRLP(i), S_{ri}, n_i, P_{cmaxi}, $fS_{lmax,}$ cp1f, cp3f, rp6f

Group 2 – JA, JB, JC, I

Input Variable	**Format**	**Description**
IRLP(i)	Integer	Relative permeability model type; -666 specifies CPVN
S_{ri}	Float	Residual saturation
n_i	Float	Initial porosity, if 0 then global variable is used instead
P_{cmaxi}	Float	Initial maximum capillary pressure at residual saturation
fS_{lmax}	Integer	Flag denoting whether the saturation at which capillary pressure goes to zero changes (0) or remains fixed at 1 (>0)
cp1f	Float	Currently non-functional flag for user-specified maximum saturation value
cp3f	Float	Currently non-functional flag for Buckles residual saturation value
rp6f	Float	Currently non-functional flag for Buckles exponent *q*

Example 1: Global variable porosity input (n_i), decreasing S_{lmax}. S_{ri} is specified at 0.1and P_{cmaxi} at 0.013 MPa. Slmax varies with porosity. The last two "1" entries are placeholders.

```
rlp
 -666  0.1  0  0.013  0  1  1

1 0 0 1
```

Example 2: User entered initial porosity n_i of 0.35, decreasing S_{lmax}.

```
rlp
  -666  0.1  0.35  0.013  0   1

1 0 0 1
```

Example 3: User entered initial porosity, S_{lmax} held fixed at 1.

```
rlp
  -666  0.1  0.35  0.013  1  1

1 0 0 1
```

Model -333: Leverett function

Input Variable	**Format**	**Description**
IRLP(i)	Integer	Relative permeability model type; -333 specifies Leverett Function
S_{ri}	Float	Residual saturation
n_i	Float	Initial porosity, if 0 then global variable is used instead
P_{cmaxi}	Float	Initial maximum capillary pressure at residual saturation
cp3f	Integer	Flag to allow changing residual saturation (1 = changing S_r, 0 = constant S_r)
rp6f	Float	Initial permeability for Leverett function (m^2)

Example 1: Leverett capillary function with changing residual saturation. Initial permeability is specified as 10^{-12} m^2.

```
rlp
 -333 0.1  0.35  0.013   1  1.e-12
1 0 0 1
```

8. Appendix B: Code for CPVN and Leverett functions implemented in FEHM

```
c * * * * * * * * * * PJJOHNSON CODE MODIFICATIONS, SUMMER 2017 * * * * * * *
c added four flags for por-dependent capillary functions
c these are tied to the linear rlp model - user assigns as normal except Slmax is given a
flag, -111, -333, -666, or -999
c which activates the f(sat, n) one
c pjn, pjni, pjsr, pjSri, pjcpmax, pjcpmaxi are variables used for that
c ALL PJJOHNSON variables used for calcs throughout FEHM are noted by prefix pj
c

                  if(irlpt(it).eq.-666) then
c set residual saturation and max capillary pressure
c                      open(666,file='Cp_out.txt')

                       pjSri= rp1f(it)
                       pjCpmaxi=cp1f(it)

c read porosity from global variables
                       pjn=ps(mi)
                      if(pjn.ge. 0.9 .or. pjn.le.1e-6) then
                          pcp(mi) = 0
                          dpcef(mi) = 0
                      else

c flag for initial porosity: if 0, then read it from global
c otherwise, user can specify value to use (e.g. for same material with different
properties)
                      if(rp5f(it) .gt. 0) then
                          pjni = rp7f(it)
                      else

                       pjni = psini(mi)
                      endif

c flag for changing saturation above which Pc = 0; if 0, change it, otherwise stays same
                      if(cp3f(it).ne.0) then
                          pjlmax = 1
                      else
                          pjlmax = 1-pjn
                      endif
c linear residual saturation calculation
                       pjSr=(pjSri/(1-pjni))*(1-pjn)

c extrapolate max capillary pressure - note that this is at sat = Sr, not sat = 0
(different from rlp 1)
c                       pjCpmax=(pjCpmaxi/pjsri)*(pjsr)
                       pjCpmax=pjCpmaxi*(1-pjn)/(1-pjni)
c read saturation
                       pjsat=s(mi)
c                         pjb = pjCpmax + (pjCpmax/(pjlmax-pjSr)*pjSr)
c calculate Pc
                       if(pjsat.ge.pjlmax) then
                           pcp(mi)=0
```

```
548                         else if(pjsat.le.pjSr) then
549                            pcp(mi)=pjCpmax
550                         else
551                           pjm = -1*(pjCpmax / (pjlmax - pjSr))
552   c define derivative
553                           pcp(mi) = pjCpmax*(pjlmax-pjsat)/(pjlmax-pjSr)
554   c
555   c
556                            dpcef(mi) = pjm
557   c
558                         end if
559                         end if
560
561
562                     else if(irlpt(it).eq. -333) then
563   c Leverett function
564
565   c if user enters a number for porosity entry in rlperm.f, use that
566   c if they enter 0, then use the global variable
567   c this allows them to have multiple different units be compared to same standard
568                     if(rp7f(it) .gt. 0) then
569                             pjni = rp7f(it)
570                         else
571
572                          pjni = psini(mi)
573
574                         endif
575   c take initial maximum capillary pressure and residual saturation from input
576                          pjCpmaxi = cp1f(it)
577
578
579                          pjSri= rp1f(it)
580   c
581   c read current porosity from global variables
582                         pjn=ps(mi)
583   c Permeability comes from salt macro, but is sometimes fed 0 (e.g. timestep 1)
584   c so address that if need be
585                          if(pjk(mi) .eq. 0) then
586                              pjk(mi) = pjki(it)
587                          endif
588
589   c Calculate leverett capillary pressure
590                          pjCpmax = pjCpmaxi*(sqrt(pjki(it)/pjni) /
591        &                 (sqrt(pjk(mi)/pjn)))
592
593                            pjlmax = 1
594
595   c handle residual saturation based on user preference
596   c if they use 0, hold Sr constant; otherwise, vary with porosity
597                        if(cp3f(it).ne.0) then
598                         pjSr=(pjSri/(1-pjni))*(1-pjn)
599
600                        else
601                            pjSr = pjSri
602                        endif
603   c truncate Sr in case it tries to go >1 or to .99999 with function divergence issues
604                         if(pjSr .ge. 0.99) then
605                             pjSr = 0.99
```

```
606                         endif
607   c read saturation
608                         pjsat=s(mi)
609   c calculate Pc
610   c max sat is currently 1 but if modified, this line handles that
611                         if(pjsat.ge.pjlmax) then
612                             pcp(mi)=0
613                             dpcef(mi)=0
614   c if Sl < Sr, use maximum value
615                         else if(pjsat.le.pjSr) then
616                            pcp(mi)=pjCpmax
617                            dpcef(mi)=0
618   c otherwise fit saturation function
619                         else
620                           pjm = -1*(pjCpmax / (pjlmax - pjSr))
621                           pcp(mi) = pjCpmax*(pjlmax-pjsat)/(pjlmax-pjSr)
622
623   c I added a truncation here to hold Pc to no more than an order of magnitude higher than
624   the starting value
625   c to avoid crashes
626                           if(pcp(mi) .gt. (10*pjCpmaxi)) then
627                               pcp(mi) = 10*pjCpmaxi
628   c failsafe in case of model crash
629                           else if (pcp(mi).lt.0) then
630                               pcp(mi) = 0
631                           else
632                               pcp(mi) = pcp(mi)
633                           end if
634
635                           pjm = -1*(pjCpmax / (pjlmax - pjSr))
636                           dpcef(mi) = pjm
637                         end if
638   c following comment lines are output files that can be activated to check calcs
639   c                     write(333,*) pjni, pjn
640   c                     write(666,*) pjki(it), pjk(mi)
641   c                     write(999,*) pjCpmaxi, pjCpmax
642   c                     write(111,*) pjSri, pjSr
643   c                     write(777,*) pjsat, pcp(mi)
644
645                         end if
646
647
648
649   c end pjjohnson changes
650
```

9. Appendix C: Paper submitted to Transport in Porous Media

The following material is in review at Transport in Porous Media. Testing of the function and the test problems described herein was conducted during the early period of the 2018 fiscal year.

Impact of a porosity-dependent retention function on simulations of porous flow

Peter J. Johnson[*1,2], George A. Zyvoloski[1], Philip H. Stauffer[1,2]*

*Corresponding author: Peter J. Johnson, MS T003, Los Alamos National Laboratory, Los Alamos, NM 87545. Tel.: (505) 667-5518, Email: pjjohnson@lanl.gov

[1]EES-16: Computational Earth Science, MS T003, Los Alamos National Laboratory, Los Alamos, NM 87545

[2]Department of Geology, The University at Buffalo (SUNY), Amherst, NY 14260

Keywords: Capillary, retention curve, porosity, numerical modeling

LA-UR-18-21075 DRAFT

Abstract

Numerical models of flow in unsaturated porous media employ a range of functions to account for capillary effects. In general, these retention functions are assigned at the beginning of the simulation and calculate capillary pressure based on saturation. However, many porous systems involve changes in porosity wherein the retention function should change during the simulation. Model runs which neglect these changes may produce unphysical results such as retention of liquid water in air-filled void spaces. We present a conceptually and numerically simple function that recalculates the retention function at each timestep based on the updated porosity. The new retention function updates the maximum capillary pressure, residual saturation, and maximum saturation prior to applying the saturation fit. We compare results from a fixed (saturation only) function and the new porosity dependent retention function through a set of two numerical *Gedankenexperiments* in salt. The new retention function corrects unphysical model behaviors and causes dramatic changes in simulation behavior relative to the fixed (saturation only) function, especially when applied to systems dominated by capillary effects. These changes result in large differences in simulated porosity, saturation, and volumetric water content. Water content results obtained using the porosity dependent retention function are inverted compared to those obtained from saturation only functions, with high-porosity nodes changing from very wet when using the saturation only retention function to very dry when using the porosity dependent retention function. These test cases suggest that dynamic retention functions in changing-porosity systems are important considerations to ensure sensible simulation results.

LIST OF VARIABLES

Variable	Description
A	Mass per unit volume
m	Subscript to denote water phase
η	Subscript to note air phase
f	Flux of subsequent phase
e	Subscript to note energy
q	Source/sink term
t	Time
S	Saturation
ρ	Density
v	Subscript to denote vapor
l	Subscript to denote liquid
n	Porosity
ū	Volumetric flux term (Darcy flux)
k	Permeability
P	Pressure
g	Gravity vector
γ	Specific internal energy for subscripted phase
C_{pr}	Specific heat capacity of rock
T	Temperature
h	Specific enthalpy
κ	Thermal conductivity

Variable	Description
R_l	Liquid relative permeability
S_l	Liquid saturation
S_{lmax}	Maximum saturation above which capillary pressure goes to 0
S_r	Residual saturation
κ_t	Temperature-dependent thermal conductivity
ic	Subscript denoting chemistry timestep
Δc	Change in moles of solid salt per weight of the solid
m_s	Molar mass of solid
D_{va}	Vapor diffusion
n_i	Initial porosity
τ	Tortuosity
S_v	Air saturation with respect to water vapor
f_{mwv}	Mass flux of water vapor
P_c	Calculated capillary pressure
W_{Mwv}	Molecular weight of water vapor
P_{cmax}	Maximum capillary pressure
P_{cmaxi}	User-specified initial maximum capillary pressure
S_{ri}	User-specified initial residual saturation
Q	Empirical exponent for Buckles (1965) residual saturation function
V_l	Liquid specific volume

Introduction

Porosity changes are common in unsaturated porous media. Examples include industrial applications such as personal hygiene tissues (e.g. Sun et al., 2015), absorbent polymers (e.g. Brandt et al., 1987), cooling systems (e.g. Jo et al., 2018) and many others. Geological systems with changing porosity are abundant and include mineral dissolution or precipitation in karst, geothermal, or hydrothermal systems (e.g. Evans and Lizarralde, 2003; Waltham et al., 2005; Ball et al., 2015), thermal or mechanical stress, (e.g. Tsang, 1999), bioturbation (e.g. Pérès et al., 1998; Gingras et al., 2012), diagenetic processes (e.g. Gluyas and Coleman, 1992), simple compaction of deposits (Boudreau and Bennett, 1999), and radiogenic waste in salt (e.g. Jordan et al., 2015a,b,c; Bourret et al., 2017). Research conducted in these areas often includes numerical modeling in the unsaturated zone.

Many numerical models of unsaturated flow employ some form of user-defined retention function which is specified at the beginning of the simulation. Capillary pressure is then determined from the local saturation and is used to calculate fluid flow. Most commonly used models follow this broad approach, such as Hydrus (Šimůnek et al., 2012), TOUGH2 (Doughty, 2013; http://esd1.lbl.gov/research/projects/tough/; c.f. Calore and Battistelli, 2003), OpenGeoSys (Kolditz et al., 2012; Wang et al., 2015), PFLOTRAN (Lichtner et al., 2015), and others. Several different formulations are commonly employed in these models including linear functions, the Brooks and Corey (1964) functions, and the van Genuchten (1980) functions. Most of these functions are designed to work with a single soil/rock type throughout a simulation, referred to herein as a fixed or saturation only retention function. However, using a single, saturation-only form can become problematic if porosity changes from the initial condition. As porosity changes, the original retention function may no longer be representative of the new local porous medium. Consider an end member thought experiment example that

clearly demonstrates incorrect model behavior: Imagine that a region of the model domain completely dissolves, attaining porosity = 1; if the retention function is not changed from its original specification, this region will maintain a non-zero capillary pressure to try to satisfy the saturation-pressure balance. In this situation, water will tend to be retained in what is effectively open air. Gravity should cause this retained water to drain from the porosity = 1 region, but the original retention function, appropriate for the initial porosity, prevents drainage.

In this paper, we describe a retention function developed to dynamically alter the capillary pressure as a function of saturation based on the updated porosity at each timestep. The function is designed to be conceptually and numerically simple to facilitate application to complex problems where model convergence may be difficult independent of the retention function. Equations are implemented in the Los Alamos National Laboratory (LANL) developed porous flow simulator FEHM (Finite Element Heat and Mass Transfer Code; Zyvoloski et al., 2012) and applied to two simple thought experiments in order to demonstrate the effects of modifying the retention function as a result of changing porosity.

Background

Porous flow simulators typically allow the user to choose from a variety of standard retention functions (e.g. linear, van Genuchten, Brooks-Corey) that vary capillary pressure (P_c) as a function of saturation (S_l). The specifics of function implementation in different models vary, but the overall structure is generally similar. At some low saturation, variously referred to as residual saturation, irreducible saturation, or critical saturation, P_c rises rapidly to some maximum value (P_{cmax}). We here refer to this low saturation end-member as the residual saturation (S_r). The other endpoint of interest is a maximum liquid saturation, S_{lmax}, above which

capillary pressure goes to zero. A linear or fit is then applied between these two points to generate a retention function or characteristic curve.

Several studies have considered capillary effects with changing porosity. Leverett (1941) developed a dimensionless parameter which, when plotted against saturation, produced a single curve for a material type. This dimensionless parameter included capillary pressure and effectively a capillary radius term as the square root of *k/n*, where k is permeability in m^2 and n is porosity. In this function, capillary pressure and permeability thus alter in response to porosity changes. A form of this theory has been implemented in the modeling software TOUGH2 (Fakcharoenphol et al., 2013),

$$P_c = P_{co}\frac{(\sqrt{k/n})_0}{\sqrt{k/n}}, \qquad \text{Eq. 1}$$

but without dynamic adjustment of the end members and with a single function of saturation applied to the resulting capillary pressure calculation. Numerous experiments have shown that capillary pressure of the wetting phase is stronger when porosity is reduced (e.g. Gallipoli et al., 2003; Nuth and Laloui, 2008; Oh and Lu, 2014). Salager et al. (2010) conducted experiments on soil and developed a 3-dimensional surface of saturation, porosity, and capillary pressure that showed increasing strength of capillary effects for equal saturation as porosity decreased. Conversely, capillary effects decrease as pore diameters increase. Open air, with a porosity *n*=1, has no capillary pressure because there is no solid grain on which fluid-solid surface interactions can apply. Sweijen et al. (2016) used combined discrete element and pore unit modeling on absorbent gel particles to generate van Genuchten curves for porosities ranging from 0.1 to 0.5. For porosities above this range, the precise nature of the decrease in pressures as porosity increases is unclear, but general trends can be identified. Theory using capillary tube or

768 spherical grain models (c.f. Lucas, 1918; Washburn, 1921; Finn, 1999; Masoodi and Pillai, 2012;
769 Sweijen et al., 2016) allows for a general intuition of the capillary changes with porosity.
770 Functions for specific materials depend on the pore geometry and the nature of the fluid-solid
771 contact (e.g. contact angle) which controls the spreading of the wetting phase across the surface
772 of the solid medium. For bundled cylindrical tubes with a fixed radius, Masoodi and Pillai
773 (2012) derived a general relationship based on the Young-Laplace equation as

774 $$P_c = 2\frac{\epsilon_l cos\theta}{r_c} \quad \text{Eq. 2}$$

775 where ϵ is the surface tension of the fluid (N/m), θ is the contact angle between the fluid and
776 solid, and r_c is the tube radius (m). If porosity increases are caused by expanding pores rather
777 than the formation of new pores, r_c will also increase, driving capillary pressure towards zero.
778 Likewise, for spherical particles, Masoodi and Pillai (2012) derived the capillary pressure as

779 $$P_c = 3\frac{1-n}{n}\frac{\epsilon_l cos\theta}{r_{sp}} \quad \text{Eq. 3}$$

780 where r_{sp} is the equivalent spherical radius. In this system, too, capillary pressure drops as
781 porosity increases and also as the radius of spherical particles increases due to the increased
782 diameter of intergranular void spaces. This provides guidance on how capillary pressure should
783 change within the model even for porosities greater than 0.5, the upper limit examined by
784 Sweijen et al. (2016).

785 The new retention function we describe in this paper makes an assumption of a consistent
786 composition and structure of the porous medium surrounding a pore, so that parameters such as
787 contact angle and pore shape are unchanging. Capillary differences therefore arise only from
788 increasing or decreasing pore diameter. In the salt scenarios considered for this work, pore

diameter is assumed to change as pores expand or contract when salt dissolves or precipitates at the perimeter of the pore. Note that this approach would require modification in systems where porosity changes include changes in the mineral phase at the pore throat margin (e.g. formation of caliche horizons in silicate soils) or where porosity is increased by formation of new pores instead of widening existing pores.

We base our porosity-dependent retention function on a simple linear retention function previously implemented within FEHM, but a similar approach could be applied to the Brooks-Corey and van Genuchten functions as well. The general form of the linear retention function is

$$P_c = P_{cmax}, \qquad S_l \le S_r$$

$$P_c = P_{cmax}\frac{S_{lmax}-S_l}{S_{lmax}-S_r}, \qquad S_r < S_l < S_{lmax} \qquad \text{Eq. 4}$$

$$P_c = 0, \qquad S_l \ge S_{lmax}$$

where P_c is the calculated capillary pressure, P_{cmax} is the specified maximum capillary pressure value, S_r is the residual saturation, S_l is current liquid saturation, and S_{lmax} is the saturation at or above which capillary pressure is zero. This function is chosen for its conceptual simplicity and also for a reduction in numerical complexity, allowing application of the new porosity-dependent function to complex multiphase heat/stress/mass flow/chemical domains where model convergence may already be challenging.

Porous flow simulator

We apply the new retention function within FEHM through code changes to appropriate subroutines (Zyvoloski et al., 2012; FEHM, 2017). FEHM has been used to simulate a wide variety of multiphase coupled heat/stress/mass flow and transport problems (e.g. Stauffer et al., 1997; Yamaguchi et al., 1990; Spinelli and Fisher, 2004; Fisher and von Herzen, 2005; Tenma et

al., 2008; Winslow et al., 2016; Birdsell et al., 2000; Arnold et al., 2003; Kelkar et al., 2013; Stauffer et al., 2005). FEHM, formulated primarily as a finite volume simulator, applies equations for conservation of mass and energy between connected volumes as:

conservation of water mass,

$$\frac{\partial A_m}{\partial t} + \nabla \cdot f_m + q_m = 0, \quad \text{Eq. 5}$$

conservation of air mass,

$$\frac{\partial A_\eta}{\partial t} + \nabla \cdot f_\eta + q_\eta = 0, \quad \text{Eq. 6}$$

and conservation of energy,

$$\frac{\partial A_e}{\partial t} + \nabla \cdot f_e + q_e = 0 \quad \text{Eq. 7}$$

where $A(m, \eta)$ are the mass per unit volume of water and air, respectively; A_e is similarly the energy per unit volume; $f(m,\eta)$ are water and air mass fluxes with units of mass per area time while $f(e)$ is energy flux; with units of energy per area time. Finally, q is the source/sink term and t is time. Water mass per unit volume A_m is given by

$$A_m = n(S_v\rho_v(1-\eta_v) + S_l\rho_l(1-\eta_l)) \quad \text{Eq. 8}$$

where S is the saturation and ρ the density of the vapor phase and liquid phase (subscripts v and l respectively); n is porosity; and η is the mass fraction of air contained in the vapor phase. Air mass per unit volume is similarly,

$$A_\eta = n(S_v\rho_v\eta_v + S_l\rho_l\eta_l) \quad \text{Eq. 9}$$

Mass fluxes for water and air are:

$$f_m = (1-\eta_v)\rho_v \bar{u}_v + (1-\eta_l)\rho_l \bar{u}_l \quad \text{Eq. 10}$$

and

$$f_\eta = n(\eta_v \rho_v \bar{u}_v + S_l \rho_l \bar{u}_l) \quad \text{Eq. 11}$$

where ū is the volumetric flux, variously known as Darcy flux, specific discharge, fictitious velocity etc. (Stauffer, 2006). Darcy's Law applies to the movement of the vapor and liquid,

$$\bar{u}_v = -\frac{k_{rv}}{\mu_v}(\nabla P_v - \rho_v g) \quad \text{Eq. 12}$$

and

$$\bar{u}_l = -\frac{k_{rl}}{\mu_l}(\nabla P_l - \rho_l g) \quad \text{Eq. 13}$$

where k_r is the relative permeability of the respective phases, P is pressure, and g is the gravitational vector.

Energy per unit volume A_e is

$$A_e = (1-n)\rho_r \gamma_r + n(S_v \rho_v \gamma_v + S_l \rho_l \gamma_l) \quad \text{Eq. 14}$$

with $\gamma_r = C_{pr}T$, and the energy flux f_e given by

$$f_e = \rho_v h_v \bar{u}_v + \rho_l h_l \bar{u}_l - \kappa \nabla T \quad \text{Eq. 15}$$

The subscript r refers to the solid matrix; γ is the specific internal energy for each respective phase; C_{pr} is specific heat; h_v and h_l are specific enthalpies; κ is effective thermal conductivity; and T is temperature. Gravitational potential energy is embedded in the liquid phase specific enthalpy definition (Stauffer et al., 2014b) in FEHM as,

$$h_l = C_p T + P_l V_l + gz \quad \text{Eq. 16}$$

where C_p is the heat capacity, T temperature, P pressure, V_l is specific volume, and z is height above a reference in the direction away from the center of mass of the gravity field. With the inclusion of potential energy, the enthalpy term is sometimes referred to as methalpy (Stauffer et al., 2014b).

Fluid density and viscosity are expressed as polynomial functions of pressure and temperature and are fit to National Bureau of Standards data (Haar et al., 1984). For mixed air/water phases within an element, the relative permeability R_l function is a linear fit given by

$$R_l = \frac{S_l - S_r}{S_{lmax} - S_r} \quad \text{Eq. 17}$$

where S_l is liquid saturation and S_r is residual saturation. Other formulations of the relative permeability function are available in FEHM but only the linear approach is implemented for the porosity-dependent retention function at the present time.

The final set of constitutive relationships concern the governing equations for dissolution, precipitation, and material properties for the porous medium. For the work described herein, the porous medium is considered as salt (pure halite) using model functions applied to previous work at the Waste Isolation Pilot Plant (WIPP; e.g. Stauffer et al., 2013; Harp et al., 2014; Stauffer et al., 2014a; Bourret et al., 2016; Bourret et al., 2017; Johnson et al., 2017). The FEHM salt functions account for the solubility with temperature of salt in brine, such that change in temperature and moisture content produce precipitation or dissolution of the porous medium that are linked to porosity and permeability changes. In addition, the salt subroutines account for temporal changes in the salt medium rock properties. These salt functions have previously been developed and tested (Stauffer et al., 2013; Harp et al., 2014; Jordan et al., 2015a,b,c; Bourret et

al., 2017) and have induced major changes in porosity in the simulated domains when three phase (brine, vapor, salt) heat pipes develop.

Munson et al. (1990) identified a temperature dependence of thermal conductivity of intact salt, κ(T), as

$$\kappa_{T-WIPP}(T) = \kappa_{T-300}(\frac{300}{T})^{1.14} \quad \text{Eq. 18}$$

where T is temperature in kelvin and κ_{T-300} is the thermal conductivity of intact salt at 300 K (5.4 $Wm^{-1}K^{-1}$). Thermal conductivity is also dependent on porosity n and was described by Gable et al. (2009), based on work inverse modeling of heat experiments conducted by Bechtold et al. (2004), at the Asse salt mine in Germany as

$$\kappa_{T-ASSE}(n) = -270n^4 + 370n^3 - 136n^2 + 1.5n + 5 \quad \text{Eq. 19}$$

A modification of this function is required for higher porosities because the fourth-order polynomial deviates from physical sensibility when $n > 0.4$, first increasing from $0.4 < n < 0.6$ and then decreasing rapidly to become negative at $n > 0.75$. Consequently, a truncation is applied to this function in the present implementation of FEHM in which thermal conductivity for $n > 0.4$ is held constant at the polynomial local minimum value. Temperature and porosity effects on thermal conductivity are combined by scaling $\kappa_{T\text{-}ASSE}$ to match $\kappa_{T\text{-}300}$ at $n = 0$,

$$\kappa_{T-300}(n) = (\frac{\kappa_{T-300}}{\kappa_{T-ASSE}(n=0)}) \times \kappa_{T-ASSE}(n) \quad \text{Eq. 20}$$

In this case, $\kappa_{T\text{-}300}$ / $\kappa_{T\text{-}ASSE}$ is 5.4/5.0 or 1.08.

Solubility of salt in water is a function of temperature derived from Sparrow (2003). In the modeled range of temperatures, solubility ranges from about 6.1 mol/kg to 6.8 mol/kg. The code calculates precipitation and dissolution of a tracer to which salt properties are assigned. We

assume that the solid matrix is salt, and that any calculated precipitation or dissolution results in a porosity change. The tracer function includes separate terms for the solid matrix and the tracer within the liquid phase; this formulation is applied to allow flexibility in applying a single tracer macro form to multiple problems. Thus, after calculating a volume change due to precipitation or dissolution, the total mol/kg of the solid phase is forced to remain constant at the value of solid salt. For the salt function, the tracer is chemically the same as the matrix, so the change in tracer concentration between liquid and solid phases describes the dissolution/precipitation of the salt. Precipitation of salt fills pore space, while dissolution increases pore space; porosity is therefore related directly to porosity in each chemistry iteration *ic* as

$$\Delta n_{ic} = -\Delta c \rho_s \text{ṁ}_s \frac{1}{\rho_{NaCl}} (1 - n_{ic}) \qquad \text{Eq. 21}$$

where Δc is the change of moles of solid salt per weight of the solid (kg), ρ_s is density of the solid (kg/m^3), $_{\dot{M}s}$ is the molar mass of the solid (kg/mol), and ρ_{NaCl} is the density of salt, with $\rho_s = \rho_{NaCl}$. Permeability is related to porosity linearly as described by Cinar et al. (2006). For numerical stability in the current function, porosity is constrained to lie between a maximum of 0.9999 and a minimum of 10^{-5}. We note that Eq. 21 here places a negative before Eq. 6 of Stauffer et al. (2013), correcting this equation to produce a decrease in porosity as the concentration of the solid phase increases.

Water vapor diffusion accounts for thermal and pressure effects described by

$$D_{va} = \tau D_{va}^{o} (P_o / P) \left(\frac{T + T_o}{T_o}\right) 1.81 \qquad \text{Eq. 22}$$

where τ is tortuosity, $D_{va}{}^{o} = 2.23 \cdot 10^{-5}$, $T_o = 273.15$ K, T is temperature (°C), P is pressure (MPa), and $P_o = 0.1$ MPa (Pruess 1991). The effective free air water vapor diffusion coefficient is then

modified based on the Millington Quirk (1961) relationship. This relationship is commonly applied as a simple gradient term based on Fick's first law,

$$J = D_{eff}\nabla C \quad \text{Eq. 23}$$

where J is the solute flux (mol/m^{2}s) and C is concentration (mol/L). The effective diffusivity D_{eff} is dependent on porosity and non-liquid fraction of the pore space, or air content $\theta_a = S_a n$, where S_a is air saturation, 1-S_l (Jury and Gardner, 1991):

$$D_{eff} = \frac{D_{free}\theta_a^{10/3}}{n^2} \quad \text{Eq. 24}$$

Combining the effective and free diffusivity terms into a tortuosity term, τ, yields

$$\tau = \frac{(S_a n)^{10/3}}{n^2} \quad \text{Eq. 25}$$

However, many porous media simulators, including FEHM, use a modification of this diffusivity for porous media (Ho and Webb, 1998),

$$D^* = \frac{D_{eff}}{S_a n} \quad \text{Eq. 26}$$

In practice, this changes the exponent in the tortuosity term from 10/3, as expressed in Eq. 22, to

$$\tau = (S_a n)^{7/3}/n^2 \quad \text{Eq. 27}$$

The measured diffusion value using the simple D_{eff} formulation must be increased by $1/\theta_a$ for use in most transient modeling, a point that is often missed and can cause an underestimate of diffusivity in modeling work when porous media properties are not included (Stauffer et al., 2009). Mass transport for diffusion of water vapor through air is driven by a concentration gradient in the bulk vapor phase (air + water vapor) as

$$f_{mwv} = -D_{va} n S_v W_{Mwv} \nabla C_{wv} \quad \text{Eq. 28}$$

where f_{mwv} is the diffusive mass flux of water vapor, W_{Mwv} is the molecular weight of water vapor (kg/mol), and C_{wv} is the moles of water vapor per cubic meter. Similarly, the non-condensible fraction of the bulk vapor phase (air) is allowed to diffuse along its concentration gradient with a diffusive mass flux as:

$$f_{ma} = -D_{va} n S_v W_{Mwa} \nabla C_a \quad \text{Eq. 29}$$

where f_{mwa} is the diffusive mass flux of air, W_{Ma} is the molecular weight of air (kg/mol), and C_{wa} is the moles of air per cubic meter. We note that a common practice in porous flow simulators, assuming binary diffusion where $f_{ma} = f_{mwv}$, can lead to non-physical model behavior and we recommend that both terms be independently calculated. This is because, in the presence of a temperature gradient, the condensable flux may not remain in the vapor phase but can condense into the liquid phase.

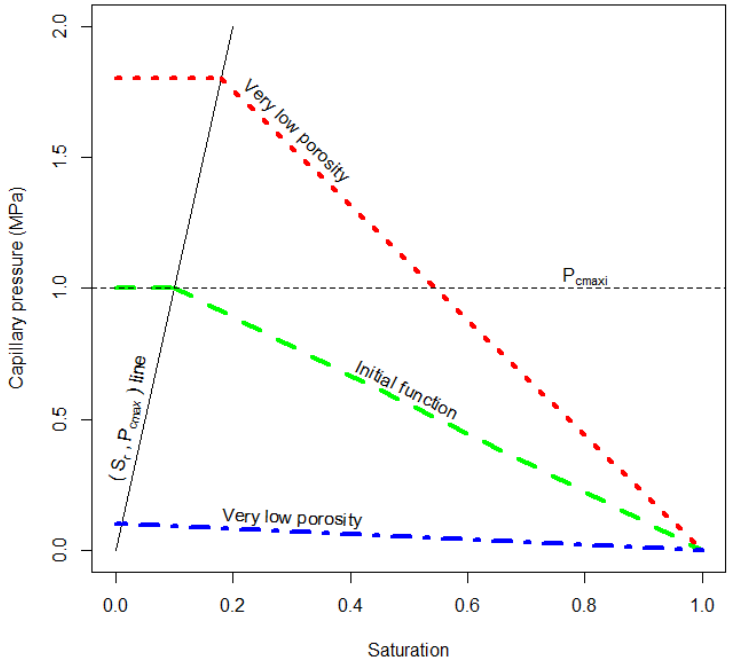

943

944 *Figure 9-1: Example of updating the retention function. The user specifies values for initial condition (residual saturation S_{ri} of 0.1,*
945 *maximum capillary pressure P_{cmaxi} of 0.3 MPa). Residual saturation and maximum capillary pressure are then recalculated based*
946 *on a linear extrapolation from (0,0) through the initially specified point. High porosity nodes then have generally very low capillary*
947 *pressures, while low porosity nodes have very high capillary pressures.*

948 ## Retention as a function of porosity and saturation: linear formulation

949 The overall objective of our new retention function is to produce a varying capillary
950 pressure curve as a function of saturation for modeling of porous media with changing porosity.
951 We therefore aim to produce stronger capillary pressure effects as porosity decreases and weaker
952 effects as porosity increases. This is done by adjusting the residual saturation (S_r) and maximum
953 capillary pressure at low saturations (P_{cmax}) values and then recalculating the retention function
954 at each timestep (Figure 1). The user inputs the initial parameters for conditions at the start of
955 the simulation. Subsequent timesteps read the updated node porosity from model global
956 variables and calculate an updated retention function at each node.

Residual saturation

In open air (*n = 1),* residual saturation is 0 and there is no capillary pressure because there is no solid grain on which wetting can occur. As porosity decreases, S_r increases. Sweijen et al. (2016) showed a weak dependency of S_r on porosity for $0.1 < n < 0.5$, but could not examine higher or lower porosity values due to their approach using packed spherical particles. Their fitted relationship was given as:

$$S_r = -1.7n^2 + n \qquad \text{Eq. 31}$$

This relationship produces negative values at porosities above about 0.588, a consequence of the spherical model constraints used in that work. The Sweijen et al. (2016) relationship also causes a reduction in residual saturation for porosities less than about 0.294, implying that more complete drainage of porous media becomes easier as porosity reduces which is generally not the case if pore characteristics other than diameter remain consistent. Conversely, Buckles (1965) and subsequent work by Holmes et al. (2009) proposed a different relationship,

$$n^Q S_r = constant \qquad \text{Eq. 32}$$

Where Q is specific to the material but generally falls close to 1. Solving for S_r yields a curve that greatly increases the residual saturation as porosity approaches 0, until S_r eventually surpasses 1. Some form of truncation to this function would be necessary to prevent unphysical residual saturation. Furthermore, this function induces steep pressure gradients as porosity approaches 0, and at very low porosity the function becomes nearly vertical so that small changes in saturation cause large differences in capillary pressure. This can present challenges to model solver routines because minor changes made to the incoming solution in each new iteration can cause instability. Depending on the specifics of the solver routines and model design, this can result in greatly increased numbers of iterations per timestep, reduction in size of

timesteps, and overall a substantial increase in runtime. In some extreme cases the instability can cause the simulation to fail to reach convergence.

In order to force a changing residual saturation while avoiding the low-porosity solver convergence issues of the Buckles (1965) formula, we apply a linear function of residual saturation with respect to porosity,

$$S_r(n) = S_{ri}\frac{1-n}{1-n_i}. \quad \text{Eq. 33}$$

This yields the appropriate residual saturation for the user-specified porosity and S_r of 0 at $n = 1$, and produces an increase in residual saturation with decreasing porosity. The linear interpolation tends to approximately match the Buckles (1965) and Sweijen et al. (2016) functions for mid-range porosities (Figure 2). The linear function avoids taking unphysical negative values at higher porosity, as in the Sweijen et al. (2016) function. The linear function tends to underestimate low-porosity residual saturation values compared to the Buckles (1965) formulation but nevertheless produces stronger capillary effects for equal saturation in the decreasing porosity case.

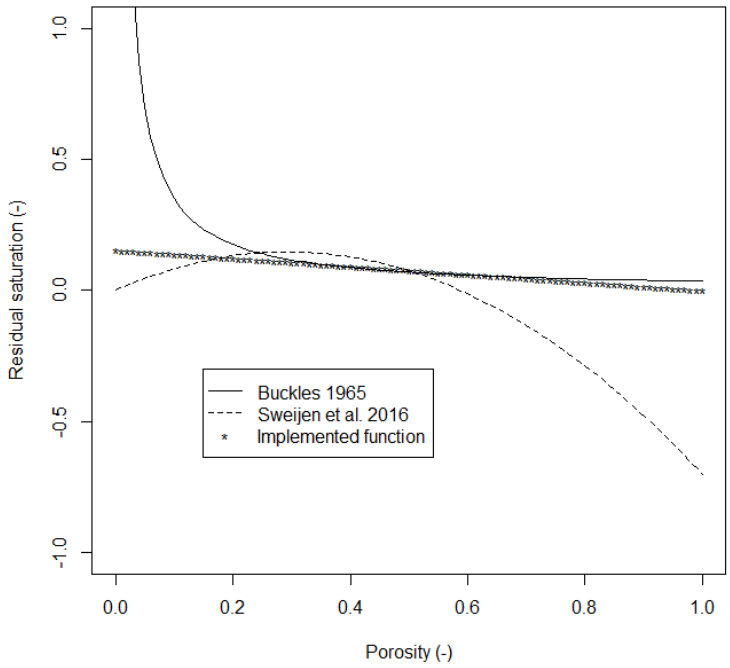

994

995 *Figure 9-2: Residual saturation (Sr) as a function of porosity (n). Equation fit (Eq. 4) based on Sweijen et al. (2016) is shown with*
996 *solid line; dashed line is function (Eq. 5) from Buckles (1965); dotted line is chosen linear function. The linear function closely*
997 *matches Buckles for porosity > 0.3 and forces increased S_r at low porosities while avoiding the steep gradient and resultant*
998 *convergence issues.*

999 ## Retention function

1000 Maximum capillary pressure will increase as pore throat diameter decreases. Similarly to
1001 residual saturation, we apply a linear fit to this value which extrapolates from P_{cmax} of 0 at n = 1
1002 through the user supplied value P_{cmaxi} at n_i to a variable calculated n = 0. In this case, the upper
1003 constraints of both P_{cmax} and the maximum residual saturation are not supplied by the user but
1004 instead determined within the model. P_{cmax} is calculated as

1005 $$P_{cmax} = P_{cmaxi}\left(\frac{1-n}{1-n_i}\right) \quad \text{Eq. 34}$$

1006 In combination, the adjusted S_r and P_{cmax} functions lead to higher capillary pressures at higher
1007 saturations when porosity decreases, and the inverse as porosity increases.

The other end point of the retention function is the saturation above which capillary forces are zero, S_{lmax}. S_{lmax} is highly dependent on the specifics of the porous medium, and a generalized formulation is difficult. For simplicity, this value is currently held at 1, but the variable is included in subsequent equations to allow for flexibility in implementation. With these endpoints established, the function is assigned as in Eq. 3 above, but with dynamic variation of the endpoints:

$$P_c = P_{cmaxi}\left(\frac{1-n}{1-n_i}\right), \qquad S_l \leq S_{ri}\frac{1-n}{1-n_i}$$

$$P_c = P_{cmax}\frac{S_{lmax}-S_l}{S_{lmax}-S_{ri}\frac{1-n}{1-n_i}}, \qquad S_{ri}\frac{1-n}{1-n_i} < S_l < S_{lmax} \qquad \text{Eq. 35}$$

$$P_c = 0.0, \qquad S_l \geq S_{lmax}$$

By keeping $\underline{P_{cmax}}$, S_r, and S_{lmax} as separate calculations within the code, the retention function can be easily altered at a later time to allow changes in how these variables are calculated.

Thought experiment examples

To demonstrate the effects of changing the retention function with porosity, we consider two numerical thought experiments in which vigorous liquid,vapor, and solute transport lead to changes in porosity. We further design these domains to feature an extensive unsaturated zone and strong capillary effects. Both domains are designed to induce large porosity changes due to high temperature gradients, the relatively high differences in solubility of salt with temperature, and abundant, continuous phase changes of brine. In the first example, we use a simple 1 m wide, 0.3 m tall 2-D radial cylinder which is heated at one end and cooled at the other similarly to the salt cylinder experiments of Olivella et al. (2011), but scaled up an order of magnitude.

Gravity is disabled for this first example. For the second example, a 10 m × 10 m square domain is used with cold top and right-hand boundaries and a heat source applied near the lower left corner. This temperature field induces convective flow of brine and vapor, gravity drainage and capillary flow, and leads to a more complex interaction between phases. Both example problems use material properties generally informed by crushed salt (Table 1). Together, these numerical thought experiments show that large differences in results occur when porosity effects are considered compared to when only an initial, single retention function is specified.

Table 9-1: Salt properties input as initial conditions for example problems

Property	**Value**	**Units**
Solid density	2165.0	kg/m^3
Specific heat capacity	931.0	J/kg·K
Permeability	1×10^{-12}	m^2
Thermal conductivity	1.1	W/m·K
Porosity	0.3	-

Heat pipe

The first domain is a 1 m long by 0.3 m tall 2-D cylinder with uniform 0.1 m grid spacing (Figure 3). Temperature is initially specified at a uniform 20°C. Note that salt capillary pressure can be quite high; Cinar et al. (2006) measured capillary pressures of >0.5 MPa in well-sorted, granular salt, so a 1 MPa maximum value is assigned for a potentially poorly-sorted salt domain. A constant temperature of 110°C is applied to the x = 0 m (left) boundary and 5°C at the x = 1 m (right) boundary. The top and bottom of the cylinder are perfect insulators and all edges are no-flow boundaries with respect to fluid flow. No sources or sinks for water are applied, with only an initial saturation of 0.5 for all nodes providing moisture. The model is run for 365 days of model time. Specifying the domain in this manner induces brine and vapor migration that causes porosity changes through dissolution and precipitation. This process has been the subject of

recent attention (c.f. Doughty and Pruess, 1990; Birkholzer, 2004; Cinar et al., 2006; Olivella et al., 2011; Caporuscio et al., 2013; Kuhlman and Malama, 2013; Jordan et al., 2015a,b,c; Stauffer et al., 2014; Rutqvist et al., 2016; Bourret et al., 2017) due to the consideration of salt as a host rock for radiogenic waste. A comprehensive discussion of brine migration in salt is beyond the scope of this paper, but a brief description of the physical mechanisms as relevant to the current work follows.

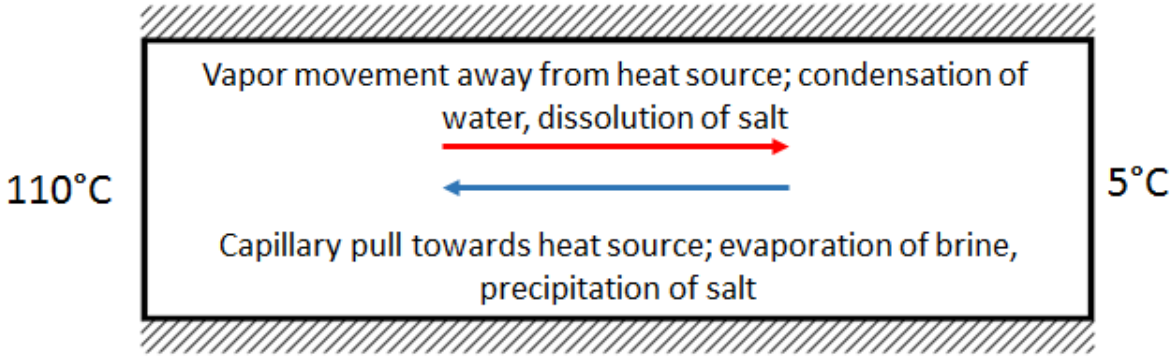

Figure 9-3: Salt cylinder domain and conceptual model. Top and bottom are no-flow, insulated boundaries. Fluid may not pass through the left or right boundaries.

Evaporation occurs at and near the heat source, oversaturating the remaining brine with respect to salt and inducing mineral precipitation. This precipitated salt reduces porosity and permeability near the heat source, leading to higher capillary pressure. Water vapor transports away from the heat source towards the cold end of the cylinder. As it does, it cools and condenses which increases the available volume of unsaturated water in cooler nodes, inducing dissolution and an increase in porosity and permeability leading to lower capillary pressure. Condensation is driven by changing water vapor pressure, the curve of which is steepest at high temperatures and is depressed by the presence of salt to about 75% of its desalinated value (Figure 4; Bourret et al., 2017). The boiling point of saline brine is raised to about 108.5°C as a

result. Water vapor pressure decreases most rapidly at high temperatures. Air moisture content (g/m^3) at 20°C is about 1/30 of that at the boiling point. This means that 29/30 of available water vapor have condensed over the distance from the location of boiling to the location of the 20 C contour. Hence, most of the porosity impacts are greatest in warm areas of the model domain. Drying of nodes near the heat source induces capillary wicking of brine to replace the water that has evaporated and drives a continuous cycle. Salt saturated water may also move into colder areas of the model where solubility is lower, causing precipitation of salt. This effect competes with condensation-induced dissolution of salt. The precise porosity change at any given node is therefore driven both by the change in total water volume and the temperature-dependent solubility of salt, both of which focus porosity increases in warm but sub-boiling areas of the model.

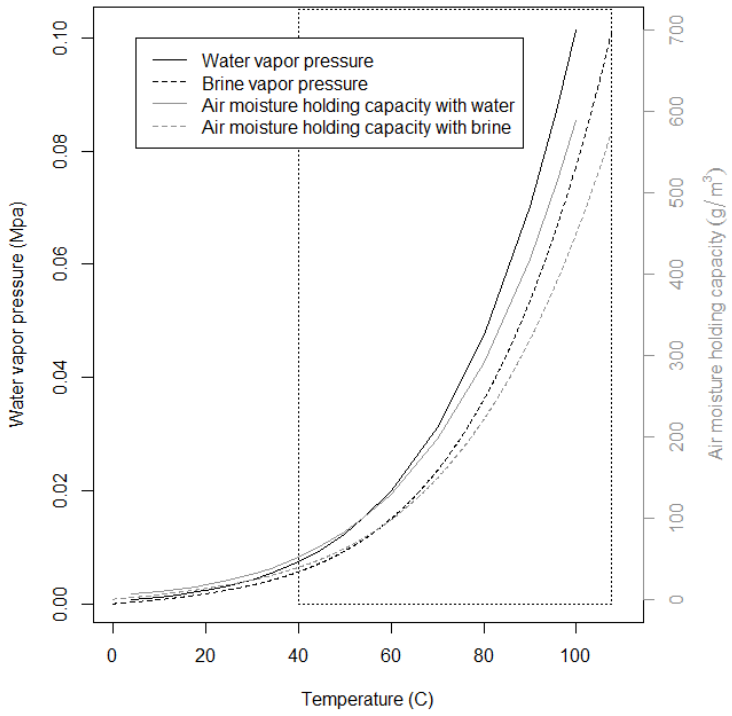

Figure 9-4: Schematic of vapor pressure curve (black) and air moisture holding capacity (gray) for pure water (solid line) and brine (dashed line). Evaporation/condensation and precipitation/dissolution reactions are strongest in the steepest parts of the curve (rectangle).

We compare results for porosity, saturation, volumetric water content as the product of porosity × saturation, and temperature (Figure 5) through the horizontal centerline of the cylinder. Porosity results follow a similar pattern between the two retention functions, with a decrease near the heat source and an increase in the middle of the cylinder where abundant water condenses. However, results using the new retention function show a much more subdued increase in porosity, with a maximum value of about 0.47 compared to total dissolution when using the fixed, saturation only retention function. Saturation results also contrast between the functions. With the fixed retention function, capillary pressure balance is achieved by equilibrating saturation throughout the domain. When using the new retention function, where capillary pressure drops as porosity increases, pressure equilibrates at different saturations for

different porosities. Specifically, high-porosity nodes must have lower saturation and low-porosity nodes must have higher saturation in order to balance capillary pressure.

As a consequence of the combination different porosity and different saturation, the two functions produce results that show highly contrasting volumetric water content. In both cases, the extremely low porosity at the heater causes low water content, but otherwise the two functions produce different outputs throughout the model domain. With equal saturation throughout, results using the saturation-only function show water content as following porosity, with most of the water concentrated in the highly porous nodes and reductions elsewhere in the domain. The porosity-dependent retention function, by contrast, causes nodes within the strong dissolution zone to be relatively dry, while water content is higher towards the cold end of the cylinder.

Temperature results for the two simulations show a marked difference in the distribution and gradients of temperatures. Total dissolution of a portion of the model domain in the simulation using the saturation-only retention function slows heat transfer through those nodes because the thermal conductivity function (Eq. 19) is truncated to a low value (~0.5 W/m K). Heat transfer in this case is dominated by movement of air and vapor and by conduction through the brine in the pore space. As a result, heat transfer is very slow through the dissolution band and a steep thermal gradient is induced. By contrast, the simulation using the porosity-dependent retention function does not allow for total dissolution at any nodes. Thermal conductivity of the remaining solid fraction remains relatively high, so that the thermal gradient is shallower and temperatures at any given point in the domain are lower that at the same point in the fixed retention function simulation.

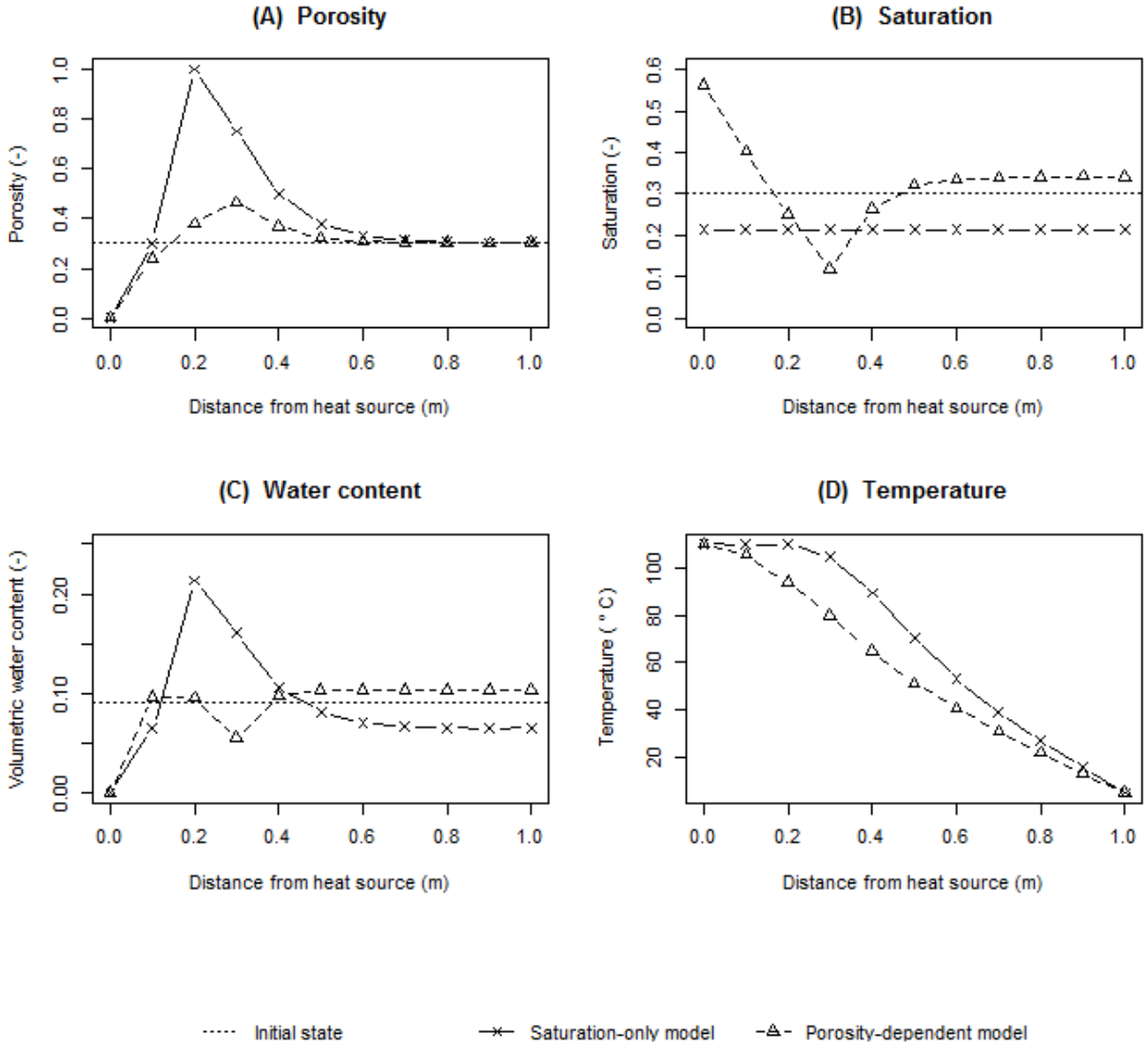

Figure 9-5: 365-day model results for porosity (A), saturation (B), water content (C), and Temperature (D). Initial condition is shown with dotted line. "X" symbols indicate results when a saturation-only retention function is used. Triangles indicate results with the new porosity-dependent retention function. Heat source is at x = 0 and cold boundary is at x = 1.

Square box

The second example scenario uses a 10 m × 10 m, 2-D square domain with 0.1 m spacing (Figure 6). As previously described, we apply the salt function built within FEHM with porous media characteristics similar to the previous run. Boundary and initial conditions are designed to induce strong changes in porosity. The bottom 8 m are fully saturated at hydrostatic pressure,

while the top 2 m are fully dry at time $t = 0$. Initial temperature in the entire domain is 20°C. The edges of the domain are no-flow boundaries with respect to mass. The top and right boundaries are held constant at 20°C. A constant temperature of 120°C is input 3 m above the origin, and gravity is enabled in this numerical experiment. The geometry of the simulation causes convective circulation. Liquid recharge at the heat source is driven by capillary pull of water from as the water near the heat source boils and increases capillary pressure near the heater. Gravitational settling of water from higher in the domain also contributes to recharge near the heater. Strong porosity changes are induced by circulating flow of vapor and liquid. The set-up of this simulation allows examination of the behavior of highly-porous nodes above the saturated water surface. 400 days of model time are simulated for each scenario.

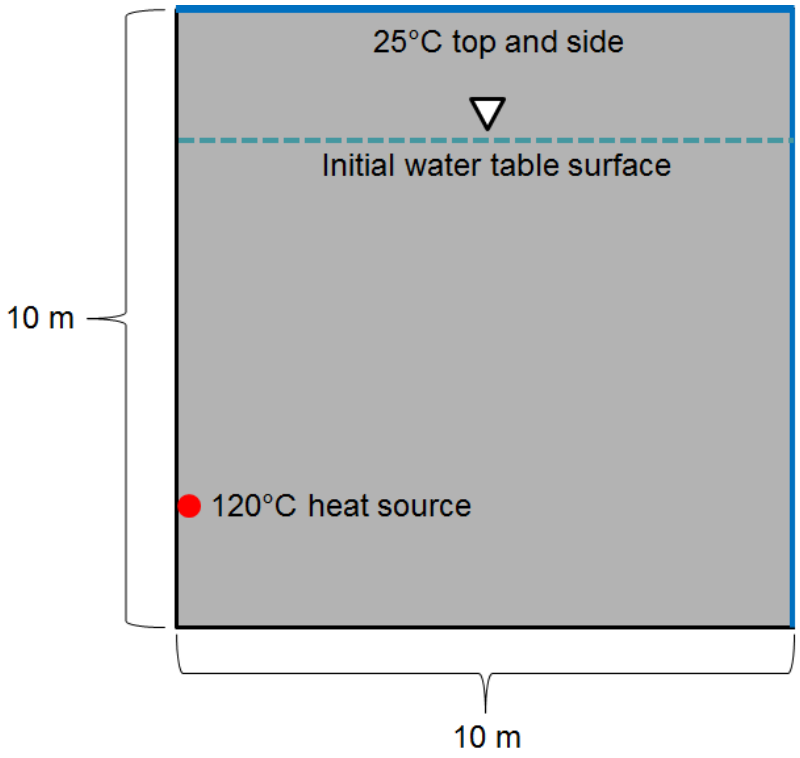

Figure 9-6: Model domain for 2D setup. The box is closed with respect to mass flow. The top and right-hand boundaries are held constant at 25°C. A constant 120°C temperature is input above the lower left corner, allowing for capillary draw of any water that accumulates below the heat source.

Results for porosity, saturation, and volumetric water content are shown in Figure 7. For both retention functions, a low-porosity rind forms near the heat source. A dissolution front forms farther from the heat source (typically about 6 m) where condensation and increased solubility of salt combine for the greatest porosity change. However, using the new retention function, the dissolution front is slightly closer to the heat source and considerably narrower. Dissolution is weaker inside the dissolution band, with total dissolution only in a 1-2 node wide band that extends from about 3 m to 8 m high in the box.

Beyond the dissolution front is a secondary band of reduced porosity, which is wide and strongly reduced when using the saturation-only retention function. This same reduced porosity band is thin and of lower intensity when using the porosity-dependent retention function. The temperature gradient at this point is very sharp for both retention functions; consequently, nearly all of the water vapor condenses in the high-porosity region where water vapor pressure changes most rapidly. Little water vapor condenses beyond the dissolution front, so most of the water entering these nodes is drawn from the porous region in the form of liquid water that is already saturated with salt. Cooling causes the water to become oversaturated and salt to precipitate, closing pore space.

When the saturation-only retention function is applied, the dominance of capillary effects with the limited available volume of water causes saturation to be distributed nearly evenly through all nodes. A slight decrease is observed at the heat source due to repeated boiling of water, as well as a hydrostatic effect with more water at the bottom of the domain. High-porosity nodes in stacked vertical arrays remain partly saturated, highlighting the problem with water being retained in void space, the issue that originally motivated the new porosity dependent retention function. By comparison, the new retention function has considerable

heterogeneity in saturation. A band of near-zero saturation forms where high-porosity nodes drain into underlying nodes. Water is no longer retained in void space in these areas. Saturation is also low in the high-porosity nodes near the base of the model because of capillary drainage into the surrounding nodes. Meanwhile, low-porosity nodes in the cooling region and near the heat source have higher saturation than the corresponding parts of the saturation-only retention function simulation due to the much stronger capillary pressure in these nodes using the porosity-dependent form of the retention function.

As with the three-phase heat pipe numerical experiments described in Section 5.1, volumetric water content shows a nearly complete inversion in the high-porosity nodes when using the new retention function. The even distribution of saturation in the saturation-only retention function causes the highly porous areas to be water-rich, with up to 80% of the represented volume filled with water. Conversely, the new retention function preferentially drains high-porosity nodes either into surrounding nodes through capillary flow or downward by gravity. Consequently, the porous nodes in the simulation using the porosity dependent retention function have very low water contents while the high porosity nodes in the simulation using the fix, saturation-only retention function have relatively high water content.

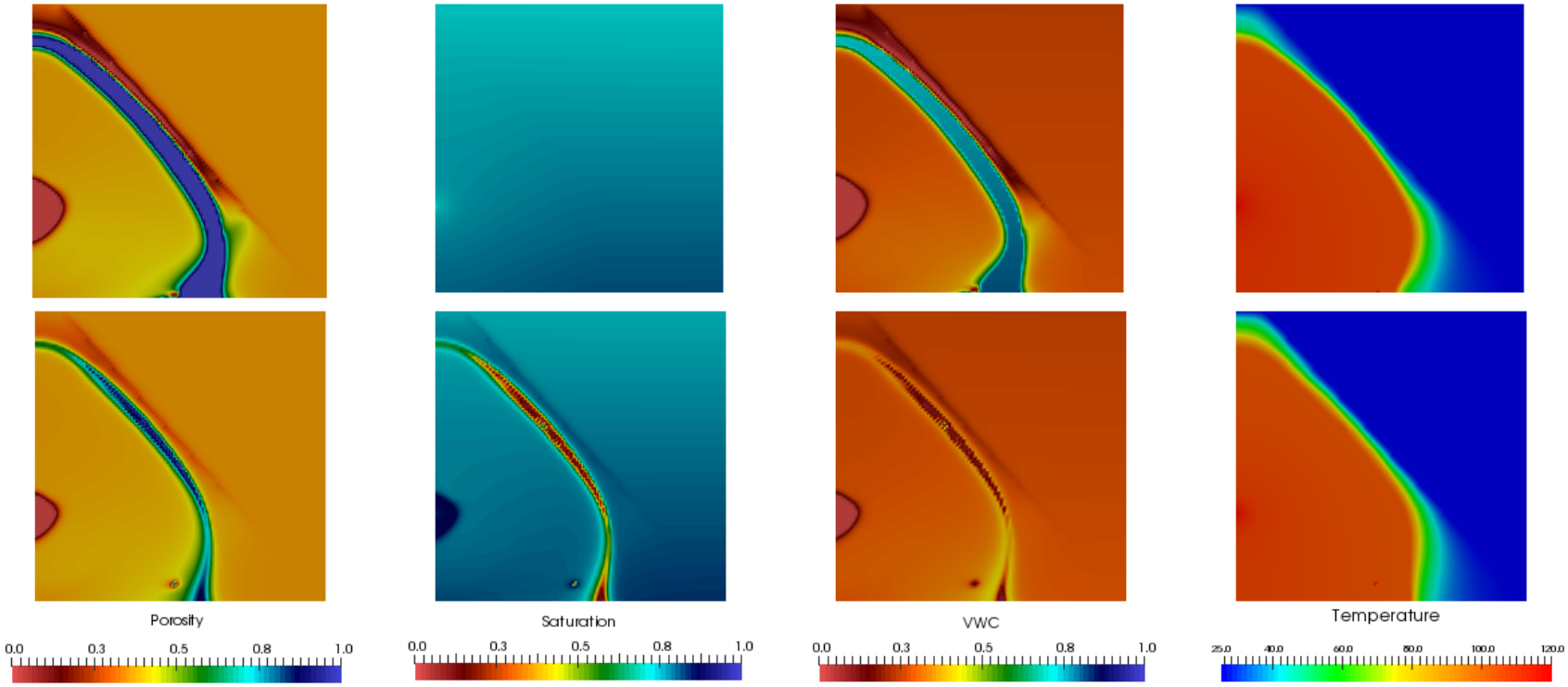

Figure 9-7: (left to right) Porosity, saturation, volumetric water content (VWC), and Temperature (°C) contours for the saturation-only retention function (top row) and new porosity-dependent retention function (Bottom row). Porosity changes are restricted in the new function because capillary pull toward the heat source is prevented by the increasing porosity region which limits capillary pressure and residual saturation. Saturation is much more heterogeneous and water is drawn into lower-porosity regions surrounding the dissolution band. As a result, water content of the porous portions of the domain is greatly reduced in the new function, compared to very high water content (and retained water) in the wide dissolution band of the saturation-only retention function.

Discussion

The two thought experiments presented above demonstrate a fundamental change in the behavior of simulated three-phase heat pipes when a porosity dependent retention function is included. When a single, saturation-only retention function is specified, pressure equilibrium is achieved by evenly distributing saturation throughout the domain; when capillary pressure is a major component of the pressure term in the system, the even distribution of saturation follows naturally from having a single retention function. As a result, water content scales with porosity, so that highly porous nodes contain large volumes of water. By contrast, the porosity-dependent retention function must vary saturation between nodes to equilibrate pressure; highly porous nodes must be dryer to have the same capillary pressure as low-porosity nodes. In fact, as porosity approaches one, capillary pressure goes to zero, resulting in no capillary pull of water towards open space.

The contrast in capillary behavior affects all types of results. Since the considered system is driven by reactions between the salt medium and water, variability in water content causes a feedback in the driving chemical reactions. In simulations using the new porosity dependent retention function, this difference manifests as a limitation on the magnitude of porosity changes, where drying of nodes with increased porosity limits further dissolution, while the saturation-only retention function forces ever-stronger changes. Water content is inverted between simulations using the two retention functions. Differences in dissolution can force changes in heat transfer due to variation in thermal conductivity and convective moisture flow. The brine migration-driven aspects of the chemical reactions are also different between the two functions, because high-porosity regions limit capillarity-driven recharge of water to the heat source; especially in the salt cylinder model. This effect is important because of the lack of gravity flow to counter reduced capillary pressure.

The porosity-dependent retention function tends to induce an increase in the saturation of the lowest-porosity nodes when compared to the saturation-only retention function. In our salt cylinder thought experiment, the saturation of the lowest-porosity node nearly tripled when porosity effects on capillary pressure were taken into account. It may be further noted that presenting volumetric water content in the absence of saturation may lead to confusion as to the presence of water within low-porosity nodes because the porosity term dominates the saturation term, for example, a near-zero volumetric water content node can have high saturation. For applications in which the saturation in pore space matters, such as calculations of relative permeability, this may lead to erroneous interpretation of model results. Furthermore, direct examination of saturation results may aid in interpreting model behavior as compared to experimental results. In any case, for simulations of porous flow with changing porosity, presenting saturation data separately from volumetric water content and porosity may be useful for understanding the system behavior.

Conclusion

We developed a new retention function that dynamically alters the capillary pressure curve for porous media that experience porosity changes. A maximum pressure and residual saturation are calculated at each timestep based on the updated node porosity. Capillary pressure is then calculated as a function of saturation based on a new capillary pressure curve ranging between residual saturation and a maximum saturation, 0 MPa pressure endpoint. The new function results in lower capillary pressures for high-porosity nodes at equal saturation as compared to low-porosity nodes, simulating stronger retention in tighter pore spaces and more complete drainage of open pores.

Two thought experiments presented in this paper illustrate how accounting for porosity dependent retention alters simulation results and the fundamental behavior of the system. Fixed, saturation-only retention functions tend to equilibrate saturation evenly throughout the domain, resulting in unphysical liquid water retained in void space. Water therefore tends to accumulate in high-porosity regions of the model domain. The presence of abundant water in highly porous nodes can further strengthen dissolution/precipitation reactions in heat pipe settings due to heating and continued flow of brine towards the heat source. The porosity-dependent retention function tends to instead draw water out of higher porosity regions into adjacent low porosity regions where capillary pressures are stronger for equal saturation. As local porosity increases, water will drain from these nodes. If sufficient porosity is attained, further flow is prevented and the heat pipe slows or stops. These two modes cause fundamental differences in simulation outputs, especially in a systems such as the numerical thought experiments in salt where chemical reactions driven in part by moisture content lead to strong three-phase heat pipes.

Based on our numerical thought experiments, large model errors may be produced if fixed, saturation-only retention functions are applied to simulations of porous media with changing porosity. We observed large differences in results for porosity, saturation, volumetric water content, temperature, and even the location at which porosity changes occur when we compared simulations using the fixed, saturation-only retention function to those using the porosity dependent retention function. These errors may be particularly problematic in scenarios where capillary effects are an important driver of the porosity changes. A porosity-dependent retention function, such as the one developed here, can improve in simulation results in such cases.

Acknowledgements

This work was undertaken in support of research funded by the DOE Office of Nuclear Energy, on grant DMS SFWD-SFWST-2017-000102.

References

Arnold, B.A., Kuzio, S.P., Robinson, B.A. Radionuclide transport simulation and uncertainty analyses with the saturated-zone site-scale model at Yucca Mountain, Nevada. J. Cont. Hyd. 62-63:401-419. (2003).

Ball, J.L., Stauffer P.H., Calder, E.S., Valentine, G.A. The hydrothermal alteration of cooling lava domes. Bulletin of Volcanology, 77(102), (2015). doi: 10.1007/s00445-015-0986-z.

Bechtold, W., Smallos, E., Heusermann, S., Bollingerfehr, W., Bazargan-Sabet, B., Rothfuchs, T., Kamlot, P., Gnupa, J., Olivella, S., Hansen, F.D. Backfilling and sealing of underground repositories for radioactive waste in salt (BAMBUS II Project). EUR 20621 EN, European Commission (2004).

Birdsell, K.H., Wolfsberg, A.V., Hollis, D., Cherry, T.A., Bower, K.M. Groundwater flow and radionuclide transport calculations for a performance assessment of a low-level waste site. J Cont Hyd 46:99-129 (2000).

Birkholzer, J.T. Estimating liquid fluxes in thermally perturbed fractured rock using measured temperature profiles. Journal of Hydrology 327(3-4), 496-515 (2004). doi:10.1016/j.jhydrol.2005.11.049.

Boudreau, B.P. and Bennett, R.H. New rheological and porosity equations for steady-state compaction. American Journal of Science 299, 517-528 (1999).

Bourret, S.M., Johnson, P.J., Zyvoloski, G.A., Chu, S.P., Weaver, D.J., Otto, S., Boukhalfa, H., Caporuscio, F.A., Jordan, A.B., Stauffer, P.H. Experiments and modeling in support of generic salt repository science. Los Alamos National Laboratory, USDOE Used Fuel Disposition Campaign Final Report (2016), LA-UR-16-27329.

Bourret, S.M., Otto, S., Johnson, P.J., Weaver, D.J., Boukhalfa, H., Stauffer, P.H. High level waste in salt repositories: Experiments and simulations of evaporation in the underground. Waste Management 2017 Proceedings (2017).

Brandt, K.A., Goldman, S.A., Inglin, T.A. Hydrogel-forming polymer compositions for use in absorbent structures. Patent, US RE362649 E (1987).

Brooks, R.H. and Corey, A.T. Hydraulic properties of porous media. Hydrology Papers, Colorado State University, Fort Collins, Colorado (1964).

Buckles, R.S. Correlating and averaging connate water saturation data. Journal of Canadian Petroleum Technology 9(1), 42-52 (1965).

Calore, C., Battistelli, A. Application of TOUGH2/EWASG to the modelling of salt water injection into a depleted geothermal reservoir: preliminary results. Conference paper, TOUGH Symposium 2003, Berkeley, CA, USA proceedings (2003).

Caporuscio, F.A., Boukhalfa, H., Cheshire, M.C., Jordan, A.B., Ding, M. Brine migration experimental studies for salt repositories. FCRD Used Fuel Disposition Campaign Milestone FCRD-UFD-2013-000204 (2013).

Cinar, Y., Pusch, G., Reitenbach, V. Petrophysical and capillary properties of compacted salt. Transport in Porous Media 65(2), 199-228 (2006).

Doughty, C., Pruess, K. A similarity solution for two-phase fluid and heat flow near high-level nuclear waste packages emplaced in porous media. International Journal of Heat and Mass Transfer 33(6): 1205–1222 (1990).

Doughty, C. Users guide for hysteretic capillary pressure and relative permeability functions in TOUGH2. Report, Lawrence Berkeley National Laboratory, Berkeley, CA, LBNL-6533E (2013).

Evans, R.L., Lizarralde, D. Geophysical evidence for karst formation associated with offshore groundwater transport: an example from North Carolina. Geochemistry, Geophysics, Geosystems 4(8) (2003).

Fakcharoenphol, P., Xiong, Y., Hu, L., Winterfield, P.H., Xu, T., Wu, Y. User's guide of TOUGH2-EGS: A coupled geomechanical and reactive geochemical simulator for fluid and heat flow in enhanced geothermal systems, version 1.0. Petroleum Engineering Department, Colorado School of Mines (2013).

FEHM (2017), FEHM Website, https://fehm.lanl.gov/ accessed Jan 11, 2017.

Finn, R. Capillary surface interfaces. Notices AMS 46(7), 770-781 (1999).

Fisher, A.T., Von Herzen, R. Models of hydrothermal circulation within 106 Ma seafloor: Constraints on the vigor of fluid circulation and crustal properties below the Madeira Abyssal Plain. Geochem Geophys Geosyst 6(11) (2005). Doi:10.1029/2005GC001013.

Gable, C.W., Clayton, D.J., Lu, Z. Inverse modeling to determine thermal properties of salt due to heating from high level waste emplaced in a generic salt repository. US DOE Office of Nuclear Fuel Recycling Report AFCI-WAST-PMO-DV-2009-000001 (2009).

Gallipoli, D., Wheeler, S., Karstunen, M. Modelling of the variation of degree of saturation in a deformable unsaturated soil. Géotechnique 53(1), 105-112 (2003).

Gingras, M.K., Baniak, G., Gordon, J., Hovikoski, J., Konhauser, K.O., La Croix, A., Lemiski. R., Mendoza, C., Pemberton, S.G., Polo, C., Zonneveld, J. Porosity and permeability in bioturbated sediments. Developments in Sedimentology 64, 837-867 (2012), http://dx.doi.org/10.1016/B978-0-444-53813-0.00027-7

Gluyas, J., Coleman, J. Material flux and porosity changes during sediment diagenesis. Nature 356(6364), 52-54 (1992).

Harp, D.R., Stauffer, P.H., Mishra, P.K., Levitt, D.G., Robinson, B.A. Modeling of high-level nuclear waste disposal in a salt repository. Nuclear Technology 187:294-307 (2014). Doi:10.13182/NT13-110

Ho, C., Webb, S. Review of porous media enhanced vapor-phase diffusion mechanisms, models, and data: Does enhanced vapor-phase diffusion exist? J. Porous Media 1:71-92 (1998).

Holmes, M., Holmes, A., Holmes, D. Relationship between porosity and water saturation: methodology to distinguish mobile from capillary bound water. AAPG Annual Convention and Exhibition, Denver, CO (2009).

Jo, H.S., An, S., Nguyen, X.H., Kim, Y.I, Bang, B., James, S.C., Choi, J., and Yoon, S.S. Modifying capillary pressure and boiling regime of micro-porous wicks textured with graphene oxide. Applied Thermal Engineering 128(5):1605-1610 (2018). https://doi.org/10.1016/j.applthermaleng.2017.09.103

Johnson, P.J., Bourret, S.M., Boukhalfa, H., Caporuscio, F.A., Zyvoloski, G.A., Weaver, D.J., Otto, S., Stauffer, P.H. Experiments and modeling to support field test design. Los Alamos National Laboratory, USDOE Fuel Cycle Research & Development Final Report (2017), LA-UR-17-27759.

Jordan, A.B., Boukhalfa, H., Caporuscio, F.A., Stauffer, P.H. Brine Transport Experiments in Run-of-Mine Salt. Los Alamos National Laboratory Report (2015a), LA-UR-15-26804.

Jordan, A.B., Zyvoloski, G.A., Weaver, D.J., Otto, S., Stauffer, P.H. Coupled Thermal-Hydrologic-Chemical Model for In-Drift Disposal Test. Los Alamos National Laboratory Report (2015b), LA-UR-15-27442.

Jordan, A.B., Boukhalfa, H., Caporuscio, F.A., Robinson, B.A., Stauffer, P.H. Hydrous Mineral Dehydration around Heat-Generating Nuclear Waste in Bedded Salt Formations. Environmental Science & Technology, 5:1-13 (2015c). DOI: 10.1021/acs.est.5b01002.

Jury, W.A., Gardner, W.R. Soil Physics. 5th ed. John Wiley & Sons, New York (1991).

Kelkar, S., Tucci, P., Srinivasan, G., Roback, R., Robinson, B., Duke, C., and Rehfeldt, K. Breakthrough of radioactive plumes in saturated volcanic rock: implications from the Yucca Mountain Site. Geofluids 13(3) (2013). Doi: 10.1111/gfl/12035

Kolditz, O., Bauer, S., Bilke, L., Böttcher, N., Delfs, J.O., Fischer, T., Görke, U.J., Kalbacher, T., Kosakowwski, G., McDermott, C.I., Park, C.H., Radu, F., Rink, K., Shao, H., Shao, H.B., Sun, F., Sun, Y.Y., Singh, A.K., Taron, J., Walther, M., Wang, W., Watanabe, N., Wu, Y., Xie, M., Xu, W., Zehner, B. OpenGeoSys: an open-source initiative for numerical simulation of thermos-hydro-mechanical/chemical (THM/C) processes in porous media. Environmental Earth Sciences (2012), http://dx.doi.org/10.1007/s12665-012-1546-x

Kuhlman, K.L., Malama, B. Brine Flow in Heated Geologic Salt. Sandia National Laboratories Report SAND2013-1944 (2013).

Leverett, M.C. Capillary Behavior in Porous Solidss. Society of Petroleum Engineers 142(1) (1941). Doi:10.2118/941152-G

Lichtner, P.C., Hammond, G.E., Lu, C., Karra, S., Bisht, G., Andre, B., Mills, R., Kumar, J. A massively parallel reactive flow and transport model for describing surface and subsurface processes. PFLOTRAN user manual, http://www.pflotran.org/docs/user_manual.pdf (2015).

Lucas, R. Rate of capillary ascension of liquids. Kollid Z. 23:15-22 (1918).

Masoodi, R., Pillai, K.M. A general formula for capillary suction-pressure in porous media. Journal of Porous Media 15(8), 775-783 (2012), DOI: 10.1615/JPorMedia.v15.i8.60.

Millington, R.J., Quirk, J.P. Permeability of porous solids. Trans Faraday Soc 57:1200-1207 (1961).

Munson, D.E., Jones, R.L., Ball, J.R., Clancy, R.M., Hoag, D.L., Petney, S.V. Overtest for simulated defense high-level waste (Room B): In situ data report (May 1984-February 1988): Waste Isolation Pilot Plant (WIPP) Thermal/Structural Interactions Program. Sandia National Labs Technical Report SAND-89-2671 (1990).

Nuth, M., Laloui, L. Advances in modelling hysteretic water retention function in deformable soils. Computers and Geotechnics 35(6), 835-844 (2008), https://doi.org/10.1016/j.compgeo.2008.08.001.

Oh, S., Lu, N. Uniqueness of the suction stress characteristic curve under different confining stress conditions. Vadose Zone Journal 13(5) (2014), DOI: 10.2136/vzj2013.04.0077.

Olivella, S., Castagna, S., Alonso, E.E., Lloret, A. Porosity variations in saline media induced by temperature gradients: experimental evidences and modeling. Transport in porous media, 90(3): 763-777 (2011).

Pérès, G., Cluzeau, D., Curmi, P., Hallaire, V. Earthworm activity and soil structure changes due to organic enrichments in vineyard systems. Biology and Fertility of Soils 27(4), 417-424 (1998).

Rutqvist, J.L., Martin, B., Molins, S., Trebotich, D., Birkholzer, J. Modeling coupled THM processes and brine migration in salt at high temperatures. UFD Document FCRD-UFD-2015-000366, LBNL-191216 (2016).

Salager, S., El Youssoufi, M.S., Saix, C. Definition and experimental determination of a soil-water retention surface. Canadian Geotechnical Journal 47(6), 609-622 (2010), https://doi.org/10.1139/T09-123

Šimůnek, J., van Genuchten, M.T., Šejna, M. HYDRUS: model use, calibration, and validation. Transactions of the American Society of Agricultural Engineers 55(4), 1261-1274 (2012), DOI: 10.13031/2013.42239.

Sparrow, B.S. Empirical equations for the thermodynamic properties of aqueous sodium chloride. Desalination 159(2):161-170 (2003). https://doi.org/10.1016/S0011-9164(03)90068-3

Spinelli, G.A., Fisher, A.T. Hydrothermal circulation within rough basement on the Juan de Fuca Ridge flank. Geochem Gephys Geosys 5(2):Q02001 (2004). doi:02010.01029/02003GC000616

Stauffer, P.H., Auer, L.H., Rosenberg, N.D. Compressible gas in porous media: A finite amplitude analysis of natural convection. Int. J. of Heat and Mass Transfer 40(7):1585-1589 (1997).

Stauffer, P.H., Birdsell, K.H., Witkowski, M.S., Hopkins, J.K. Vadose zone transport of 1,1,1-trichloroethane. Vadoze Zone Journal 4(3), 760-773 (2005).

Stauffer, P.H., Vrugh, J.A., Turin, H.J., Gable, C.W., Soll, W.E. Untangling diffusion from advection in unsaturated porous media: Experimental data, modeling, and parameter uncertainty. Vadose Zone Journal 8(2):510-522 (2009). Doi:10.2136/vzj2008.0055.

Stauffer, P.H., Harp, D.R., Jordan, A.B., Lu, Z., Kelkar, S., Kang, Q., Ten Cate, J., Boukhalfa, H., Labyed, Y., Reimus, P.W., Caporuscio, F.A., Miller, T.A., Robinson, B.A. Coupled model for heat and water transport in a high level waste repository in salt. Los Alamos National Laboratory, DOE Level 2 Milestone FCRD-UFD-2013-000206 (2013), LA-UR-13-27584.

Stauffer, P.H., Jordan, A.B., Lu, Z., Zyvoloski, G.A., Boukhalfa, H., Caporuscio, F.A., Miller, T.A., Robinson, B.A. Thermo-hydrological and chemical (THC) modeling to support field test design. Los Alamos National Laboratory Document, Milestone M4FT-14LA0818064 (2014a), LA-UR 14-27548.

Stauffer, P.H., Lewis, K.C., Stein, J.S., Travis, B.J., Lichtner, P., Zyvoloski, G.A. Joule-Thomson effects on the flow of liquid water. Transport in Porous Media 105(3) (2014), DOI 10.1007/s11242-014-0379-3

Sun, Y., Kharaghani, A., Metzger, T., Müller, J., Tsotsas, E. Lotion distribution in wet wipes investigated by pore network simulation and X-ray micro tomography. Transport in Porous Media 107(2), 449-468 (2015).

Sweijen, T., Nikooee, E., Hassanizadeh, S.M., Chareyre, B. The effects of swelling and porosity change on capillarity: DEM coupled with a pore-unit assembly method. Transport in Porous Media 115, 207-226 (2016). DOI 10.1007/s11242-016-0689-8.

Tenma, N., Yamaguchi, T., Zyvoloski, G. The Hijiori Hot Dry Rock test site, Japan: Evaluation and optimization of heat extraction from a two-layered reservoir. Geotherm 37:19-52 (2008). Doi:10.1016/j.geothermics.2007.11.002

Tsang, C. Linking thermal, hydrological, and mechanical processes in fractured rocks. Annual Review of Earth and Planetary Sciences 27:359-384 (1999), https://doi.org/10.1146/annurev.earth.27.1.359.

Van Genuchten, M.T. A closed-form equation for predicting the hydraulic conductivity of unsaturated soils. Soil Science Society of America Journal 44(5) (1980).

Waltham, T., Bell, F.G., Culshaw, M.G. Rocks, dissolution, and karst, *in* Sinkholes and Subsidence. Karst and Cavernous Rocks in Engineering and Construction. Springer, Berlin, Heidelberg (2005), doi: https://doi.org/10.1007/3-540-26953-3_1.

Wang, W., Fischer, T., Zehner, B., Böttcher, N., Görke, U.J., Kolditz, O. A parallel finite element method for two-phase flow processes in porous media: OpenGeoSys with PETSc. Environmental Earth Sciences, 73(5), 2269-2285 (2015), http://dx.doi.org/10..1007/s12665-014-3576-z

Washburn, E.V. The dynamics of capillary flow. Physical Reviews 17:273-283 (1921).

Winslow, D.M., Fisher, A.T., Stauffer, P.H., Gable, C.W., Zyvoloski, G.A. Three-dimensional modeling of outcrop-to-outcrop hydrothermal circulation on the eastern flank of the Juan de Fuca Ridge. J Geophys. Res. Solid Earth 121(3) (2016), doi:10.1002/2015JB012606

Yamaguchi, T., Kunyagawa, M., Sato, Y., Oikawa, Y., Kobayashi, H., Matsunaga, I., Zyvoloski, G. Heat extraction test from hot dry rock and reservoir modeling. J. Geothermal Res. Soc. Japan 13:73-93 (1991).

Zyvoloski, G.A., Robinson, B.A., Dash, Z.V., Kelkar, S., Viswanathan, H.S., Pawar, R.J., Stauffer, P.H., Miller, T.A., Chu, S.P. Software users manual (UM) for the FEHM Application Version 3.1-3.X, LANL Report (2012), LA-UR-12-24493